J. Mech. Phys. Solids 153 (2021) 104469

Contents lists available at ScienceDirect

Journal of the Mechanics and Physics of Solids

journal homepage: www.elsevier.com/locate/jmps

# Peridynamic modelling of blasting induced rock fractures

Fan Zhu, Jidong Zhao *

*Department of Civil and Environmental Engineering, The Hong Kong University of Science and Technology, Hong Kong SAR, China*

ARTICLE INFO

*Keywords:*
Peridynamics
Blasting
Rock fracture
Plasticity
Strain rate

ABSTRACT

This paper presents a peridynamics-based computational approach for modelling blasting induced rock fractures. A new non-ordinary state-based peridynamics approach is proposed in conjunction with a Johnson-Holmquist (JH2) constitutive model to consider the pressure dependency, strain rate effect, and viscoplasticity of rocks under blasting loads. The fracturing process in a rock is assessed based on both the JH2 damage model and a tension failure model. The former evaluates the material response pertaining to excessive plastic strain and the latter is used to gauge failure based on tensile stress in consideration of strain rate effect. Detonation in the explosives is simulated using updated Lagrangian peridynamics in conjunction with Jones-Wilkins-Lee (JWL) equation of state. Simulations of single-hole blasting in granite rock are presented and compared with experimental records. The proposed approach is shown to capture reasonably well the plastic material failure surrounding the borehole as well as the tensile cracks on both radial and circumferential directions. Further sensitivity studies indicate that the intact strength parameters in the JH2 model and the tensile strength of material play a vital role in producing the obtained fracture patterns and should hereby be selected with care. The presented computational approach offers a rigorous basis for future development of versatile, multi-physics-integrated computational framework on rock blasting simulations.

## 1. Introduction

In geotechnical engineering and mining industry, blasting has been a primary means for rock excavation where explosives are charged and detonated in pre-drilled holes (Zhang, 2016). Blasting is known to generate extreme transient pressure which causes heavy fragmentation of the rock mass surrounding the drillhole. Stress waves are generated and propagate in the surrounding rock mass, triggering tensile type fractures. In industrial operations, blasting is often designed at multiple drillholes with a specified detonation sequence. The course of fracturing in rock involves the development of significant discontinuity features such as crack branching, jointing, intervening, and arresting. Numerical modelling of the blasting induced fracturing process has been widely considered a challenging task owning to the complexity of the physical processes. Quantification of blasting induced rock fractures remains largely empirical in practice. For example, the extent of blasting-induced damage zone, which is of great practical interest, has often been estimated based on peak particle velocity (PPV) (Holmberg and Persson, 1978, 1980; Mojitabai and Beatie, 1996) or detonation pressure (Hustrulid, 2010; Drukovanyi et al., 1976) through empirical formulas.

Rapid developments in both computational methodologies and computing power in the recent decades have driven the wide use of numerical means to quantify blasting induced fractures in rocks. The various numerical methods can generally be classified into

* Corresponding author.
*E-mail address:* jzhao@ust.hk (J. Zhao).

https://doi.org/10.1016/j.jmps.2021.104469
Received 17 January 2021; Received in revised form 11 April 2021; Accepted 26 April 2021
Available online 8 May 2021

continuum-based, discrete-based, and coupled approaches. The continuum-based approach features the use of popular numerical methods such as finite element method (FEM) or its variants such as extended finite element method (XFEM) and arbitrary Lagrangian Eulerian (ALE) method with a constitutive model that is capable of handling blasting induced material response (Banadaki and Mohanty, 2012; Banadaki, 2010; Ma and An, 2008; Wang et al., 2018; Wei et al., 2009; Yi et al., 2017). A number of constitutive models have been developed to quantify the viscoplastic response of rock under extreme pressure and high strain rate, including the Johnson–Holmquist (JH2) model (Johnson and Holmquist, 1994), the Holmquist-Johnson-Cook (HJC) model (Holmquist et al., 1993), the Talyor-Chen-Kuszmaul (TCK) model (Taylor et al., 1986), and the Johnson-Holmquist-Rock (JHR) model (Xie et al., 2019), with the JH2 model being perhaps the prevailing one. However, the traditional FEM method is known to experience difficulties when handling fractures and discontinuities which require mesh updating based on the geometry of discontinuities. The XFEM offers a viable way to handle fractures in the FEM framework by introducing enrichment functions to describe the displacement field (Baydoun and Fries, 2012), but either explicit or implicit description of cracks in the 3D domain may lead to overwhelming computational cost when dealing with complex discontinuity features. A cracking-particle method was proposed by Rabczuk and Belytschko (2007) in which the fractures are quantified by a collection of cracked particles so that no explicit representation of crack surface is needed, which greatly simplifies the computation and enhances the efficiency. The method was further extended with a mixed Lagrangian-Eulerian formulation to deal with large deformation problems such as impact and blasting (Rabczuk et al., 2010). The discrete-based approaches treat the rock mass as bonded discrete elements (Donzé et al., 1997; Deng et al., 2014; Lanari and Fakhimi, 2015) and simulate fracturing by allowing the bond to break. These approaches have no difficulty in handling discontinuities, but they commonly require extensive calibration of the bond parameters to render representative of a continuum media. It is also debatable whether the discrete-based approaches can faithfully handle the complex material responses under blasting load as a boundary value problem. Discrete methods are nonetheless more suitable for simulating blasting in granular media such as sand (Børvik et al., 2011). The coupled approach attempts to utilise the advantage of each of the coupling methods. For example, the coupled FEM-DEM approach (Zárate et al., 2018) uses FEM for modelling a continuum field and the discrete elements are inserted with growth of cracks. In addition to traditional methods, application of mesh free methods such as smoothed particle hydrodynamics (SPH) has become popular in the modelling of blasting induced fractures. The SPH was applied for modelling rock blasting problems with promising results shown (Gharehdash et al., 2020). The Eulerian kernel in SPH makes it suitable for handling large deformations. Nonetheless, to overcome the well-known instability issue, SPH may have to incur artificial stress corrections (Xiao and Belytschko, 2005).

Peridynamics (PD) theory (Silling et al., 2007) has recently emerged as an alternative formulation of the classical continuum mechanics. Unlike the traditional, FEM based methods, PD does not involve differentiation of the displacement field and therefore is inherently suitable for handling discontinuities. It has been applied for simulation of fracture related problems for geomaterials (Lai et al., 2015; Rabczuk and Ren, 2017; Zhu and Zhao, 2019; Gao et al., 2020) and impact/blasting problems (Madenci and Oterkus, 2014; Ren et al., 2014; Fan et al., 2016; Fan and Li, 2017) with promising results. Lai et al. (2018) have pioneered in using the PD method with the JH2 model in modelling edge-on impact and drop-ball impact problems where the material failure under extreme pressure and strain rate is shown to be reasonably captured. Hybrid method that couples the PD and SPH theories was established (Ren et al., 2014; Fan et al., 2016; Fan and Li, 2017) for modelling blasting induced fragmentation is soils where the explosive gas was simulated by SPH and classical constitutive models of soils are implemented in the PD theory. In the PD method, a continuum domain is described by material points which interact through peridynamic bonds and the fracture is modelled through bond rupture. *Bond-based peridynamics* (BBPD) (Silling, 2000) has been an early version of PD where the bonds are modelled by elastic springs independent of each other. The BBPD has restrictions on the type of materials it can handle and is usually applied to elastic material with a Poisson's ratio of 0.25. The later developed *state-based peridynamics* (SBPD) (Silling et al., 2007) has overcome the limitations in BBPD by introducing the concept of force state. The SBPD can be further divided into *ordinary* type (OSB PD) and *non-ordinary* type (NOSB PD). The former is a pure peridynamic formulation which does not involve the concept of stress and strain, whereas the latter connects the engineering stress and strain to the PD formulation. The advantage of NOSB PD is evident as it inherits the capacity of PD in handling discontinuities while allowing convenient implementations of existing constitutive and failure models in classical continuum mechanics for various materials and loading scenarios. In view of these, we employ the NOSB PD theory as the base framework in this paper to model blasting induced fractures in rock. The material response will be modelled with the JH2 constitutive model. Different types of fractures are handled by the JH2 damage model in conjunction with a tension failure model.

The traditional peridynamics is based on the total Lagrangian formulation where the interaction of material points is computed based on an undeformed reference configuration, with an underlying assumption of small deformation within the material domain. Recently, an updated Lagrangian formulation, or sometimes referred to as Eulerian formulation, has been proposed to simulate processes that involve large deformation or fluids (Silling et al., 2017; Bergel and Li, 2016; Behzadinasab and Foster, 2020). In the updated Lagrangian formulation, the neighbourhood of a material point is updated according to the deformation and the material response is assessed based on the current deformed configuration. In the present study, the updated Lagrangian formulation of NOSB PD is employed to model the explosive gas with application of the Jones–Wilkins–Lee (JWL) equation of state to offer a rigorous quantification of blasting load. The total and updated Lagrandian formulations of peridynamics are conveniently coupled to allow the blasting load being applied on the surrounding rock mass.

The paper is organised as follows. In Section 2, the formulation and implementation procedures of the computational approach are described, including the NOSB PD, the JH2 constitutive and damage model, the tension failure model, an artificial viscosity introduced to maintain numerical stability, and details in handling point damage, bond breakage and modelling explosives. In Section 3, a single-hole blasting in granite rock is simulated and validated, followed by a sensitivity study on the discretisation and major parameters. Presented in Section 4 are some concluding remarks and outlooks. The paper is intended to serve as a basis for future work on the peridynamics-based approaches on modelling blasting induced fractures.

## 2. Methodology

### 2.1. Non-ordinary state based peridynamics

In peridynamics, the material domain is first discretised into material points. For each material point, a *family* is defined by a *horizon* which is a radius representing a spherical space. All material points within the family are called neighbours. A material point is set to interact with all its neighbours through peridynamic bonds. In NOSB PD, the equation of motion at each material point can be expressed by:

$$\rho(\boldsymbol{x})\ddot{\boldsymbol{u}}(\boldsymbol{x},t)+\boldsymbol{T}_v(\boldsymbol{x},t)=\int_{\Omega_x}\left[\boldsymbol{T}(\boldsymbol{x},t)<\mathbf{x}^{'}-\mathbf{x}>-\boldsymbol{T}(\boldsymbol{x}^{'},t)\langle\boldsymbol{x}-\boldsymbol{x}^{'}\rangle+\boldsymbol{f}_{hg}+\boldsymbol{f}_c\right]dV_{x^{'}}+\boldsymbol{b}(\boldsymbol{x},t) \tag{1}$$

where $\rho$ represents material density, $\boldsymbol{u}$ represents point deformation, $\Omega_x$ defines the *family* of point $\boldsymbol{x}$ and $V_{x'}$ represents the volume of a neighbouring point. $\boldsymbol{b}$ denotes body force density. $\boldsymbol{f}_{hg}$ is an Hourglass force term to correct zero-energy mode which will be described later in this section. $\boldsymbol{f}_c$ represents a contact force term as described in Section 2.4. $\boldsymbol{T}_v$ is an artificial viscous force density to improve numerical stability as described in Section 2.5. $\boldsymbol{T}$ presents a force state that maps the bond deformation into bond force density. The total bond force density at a material point is obtained by summarising force densities of all neighbouring bonds. In NOSB PD, the force state of a bond $\boldsymbol{\xi}=\boldsymbol{x}^{'}-\boldsymbol{x}$ is computed by

$$\boldsymbol{T}<\mathbf{x}^{'}-\mathbf{x}>=\omega\langle\parallel\boldsymbol{\xi}\parallel\rangle\boldsymbol{P}_x\boldsymbol{K}_x^{-1}\boldsymbol{\xi} \tag{2}$$

where $\omega\langle\parallel\boldsymbol{\xi}\parallel\rangle$ is the value of influence function at bond $\boldsymbol{\xi}$. In the present study, the influence function is selected to be $\omega\langle\parallel\boldsymbol{\xi}\parallel\rangle=(\delta-\parallel\boldsymbol{\xi}\parallel)^2$ where the horizon $\delta$ is selected as three times the element size. By default, the bond length should be less than the horizon, so the value of the influence function reduces with increasing bond length. This form of influence function is known to have a positive second derivative and improves numerical stability (Silling et al., 2017). $\boldsymbol{P}_x$ is the first Piola-Kirchhoff stress tensor and $\boldsymbol{K}_x$ is a non-local shape tensor. $\boldsymbol{x}$ denotes the point at which the tensor is calculated. $\boldsymbol{P}_x$ and $\boldsymbol{K}_x$ are computed by

$$\boldsymbol{P}_x=\det(\boldsymbol{F}_x)\boldsymbol{\sigma}_x\boldsymbol{F}_x^{-1} \tag{3}$$

$$\boldsymbol{K}_x=\int_{\Omega_x}\omega\langle\parallel\boldsymbol{\xi}\parallel\rangle\boldsymbol{\xi}\otimes\boldsymbol{\xi}dV_{x'} \tag{4}$$

where $\boldsymbol{\sigma}_x$ refers to the Cauchy stress tensor and $\boldsymbol{F}_x$ is the deformation gradient tensor. $\det(\boldsymbol{F}_x)$ calculates the determinant of $\boldsymbol{F}_x$. The symbol $\otimes$ denotes dyadic product between two vectors. In the NOSB PD, the deformation gradient tensor is defined in a non-local form by

$$\boldsymbol{F}_x=\left[\int_{\Omega_x}\omega\langle\parallel\boldsymbol{\xi}\parallel\rangle\boldsymbol{Y}\otimes\boldsymbol{\xi}dV_{x'}\right]\boldsymbol{K}_x^{-1} \tag{5}$$

where $\boldsymbol{Y}$ represents the deformed bond vector.

The Cauchy stress is obtained based on the JH2 constitutive model described in the subsequent section. As an input to the constitutive model, the unrotated rate of deformation tensor, $\boldsymbol{d}_x$, must be computed within the framework of NOSB PD. It is computed by

$$\boldsymbol{d}_x=\boldsymbol{R}_{x(t)}^T\boldsymbol{D}_x\boldsymbol{R}_{x(t)} \tag{6}$$

where $\boldsymbol{D}_x$ is the rotated rate of deformation tensor at point $\boldsymbol{x}$ as calculated by Eq. (11). $\boldsymbol{R}_{x(t)}$ represents the rotation tensor at point $\boldsymbol{x}$ and time $t$. It is initially set as an identity tensor and updated at each time step. Updating the rotation tensor follows Flanagan and Taylor (1987) as:

$$\boldsymbol{R}_{x(t)}=\left[\boldsymbol{I}+\frac{sin(\Delta t\Omega)}{\Omega}\boldsymbol{\Omega}-\frac{1-cos(\Delta t\Omega)}{\Omega^2}\boldsymbol{\Omega}^2\right]\boldsymbol{R}_{x(t-\Delta t)} \tag{7}$$

where $\boldsymbol{I}$ is an identity matrix and the tensor $\boldsymbol{\Omega}$ is defined by $\Omega_{ij}=e_{ijk}\varpi_k$ where $e_{ijk}$ is the permutation tensor. The vector $\varpi$ is calculated by:

$$\varpi=\boldsymbol{w}+[\boldsymbol{I}\,tr(\boldsymbol{V})-\boldsymbol{V}]^{-1}\boldsymbol{\chi} \tag{8}$$

$$\boldsymbol{w}=-\frac{1}{2}e_{ijk}W_{jk}e_i \tag{9}$$

$$\boldsymbol{\chi}=e_{ijk}D_{jm}V_{mk}e_i \tag{10}$$

In Eqs. (8) through (10), $\boldsymbol{V}$ denotes the left stretch tensor. $\boldsymbol{D}$ and $\boldsymbol{W}$ are the symmetric and anti-symmetric part of the spatial velocity

gradient tensor, $\boldsymbol{L}$, as expressed by

$$\boldsymbol{D}_x = \frac{1}{2}\left(\boldsymbol{L}_x + \boldsymbol{L}_x^T\right), \quad \boldsymbol{W}_x = \frac{1}{2}\left(\boldsymbol{L}_x - \boldsymbol{L}_x^T\right) \tag{11}$$

$$\boldsymbol{L}_x = \dot{\boldsymbol{F}}_x \boldsymbol{F}_x^{-1} \tag{12}$$

where $\dot{\boldsymbol{F}}_x$ is the time derivative of the deformation gradient tensor computed by

$$\dot{\boldsymbol{F}}_x = \left[\int_{\Omega_x} \omega\langle \| \boldsymbol{\xi} \| \rangle \dot{\boldsymbol{Y}} \otimes \boldsymbol{\xi} dV_{x'}\right] \boldsymbol{K}_x^{-1} \tag{13}$$

in which $\dot{\boldsymbol{Y}}$ is the time derivative of the deformed bond vector. The left stretch tensor $\boldsymbol{V}$ is updated at each time step following

$$\boldsymbol{V}_t = \boldsymbol{V}_{t-\Delta t} + \Delta t \cdot \dot{\boldsymbol{V}}_t \tag{14}$$

where $\dot{\boldsymbol{V}}_t = \boldsymbol{L}\boldsymbol{V}_t - \boldsymbol{V}_t\boldsymbol{\Omega}$ is a rate of stretch tensor. The left stretch tensor is set to an identity matrix at the beginning of the simulation.

In the NOSB PD, the shape tensor and deformation gradient tensor must be invertible to avoid numerical singularities. For a 3D model this requires that a material point must have at least three neighbouring points and the three bonds must not be on the same plane (Warren et al., 2009). This is usually not a concern since a material point has hundreds of neighbouring points assuming a horizon of three times the element size. The issue may arise when bond breakage is modelled and points near a propagating crack may be found not having sufficient bonds to form an invertible shape tensor. In that case (very rare in our simulation though), the bond force density is directly computed as if the bond is an elastic spring, as $\boldsymbol{f} = \omega\langle \| \boldsymbol{\xi} \| \rangle (18k)/(\pi\delta^4)\boldsymbol{Y}/\| \boldsymbol{Y} \|$ where $k$ represents the bulk modulus of the material.

The NOSB PD is known to have potential problem of zero-energy mode when the net effect from all neighbouring points on the deformation gradient is zero. This is similar to the hourglass mode in the FEM. There are various ways to alleviate the zero-energy mode (Tupek and Radovitzky, 2014; Littlewood, 2011; Ren et al., 2020), amongst which a common one is to apply a penalty force at bonds that are susceptible to the zero-energy mode. In the present study, the penalty term is defined following Ren et al. (2020) as

$$\boldsymbol{f}_{hg} = \frac{2c}{tr(\boldsymbol{K}_x)}(\boldsymbol{Y} - \boldsymbol{F}_x\boldsymbol{\xi}) \tag{15}$$

where $c$ is a penalty coefficient taken as 0.01. The penalty term represents a bond force density and is added to the force state in Eq. (1).

Time integration in the NOSB PD is implemented with an explicit velocity-Verlet scheme. It follows a second order central difference algorithm, as expressed by:

$$\dot{\boldsymbol{u}}_{t+1/2\Delta t} = \dot{\boldsymbol{u}}_t + \frac{1}{2}\ddot{\boldsymbol{u}}_t \Delta t \tag{16}$$

$$\boldsymbol{u}_{t+\Delta t} = \boldsymbol{u}_t + \dot{\boldsymbol{u}}_{t+1/2\Delta t}\Delta t \tag{17}$$

$$\dot{\boldsymbol{u}}_{t+\Delta t} = \dot{\boldsymbol{u}}_{t+1/2\Delta t} + \frac{1}{2}\ddot{\boldsymbol{u}}_{t+1/2\Delta t}\Delta t \tag{18}$$

where $\Delta t$ represents the time step size. At each step, the velocity is first advanced by a half-step and the position is updated before the velocity is advanced to the next full step.

### 2.2. JH2 constitutive and damage model

The improved Johnson-Holmquist model, often referred to as the JH2 model, is selected in this study to model the response of rock subjected to blasting. The model assumes that a material is initially linear elastic until the equivalent stress reaches the yielding point. Once the material yields, a gradual softening of the material is modelled until fracture failure. The JH2 model is known to improve the original Johnson-Holmquist model by introducing a gradual softening with increasing plastic strain (Johnson and Holmquist, 1994). The formulation and implementation of the JH2 model are descried as follows.

First, the Cauchy stress tensor at each material point is updated at each time step assuming a linear elastic response:

$$\boldsymbol{\sigma}'_t = \boldsymbol{\sigma}_{t-\Delta t} + 2G(\Delta\boldsymbol{\varepsilon}) + \lambda\boldsymbol{I}(\Delta\varepsilon_{ii}) \tag{19}$$

where $\Delta\boldsymbol{\varepsilon} = \boldsymbol{d}\Delta t$ is the incremental strain tensor and $\boldsymbol{d}$ is the rate of deformation tensor obtained from Eq. (6). $\lambda$ and $G$ are the Lame constant and shear modulus, respectively. The equivalent von Mises stress is chosen as a scalar representation of the stress level. It is obtained by

$$s = \sqrt{\frac{3}{2}\sigma_{ij}^d\sigma_{ij}^d} \tag{20}$$

where $\sigma_{ij}^{d}$ denotes the deviatoric part of the current step stress tensor $\boldsymbol{\sigma}_t^{'}$ calculated in Eq. (19). The assumption on linear elastic material response is checked by comparing the equivalent von Mises stress with the yield strength. In the JH2 model, the normalized yield strength is calculated by

$$\sigma_y^* = \sigma_i^* - D\left(\sigma_i^* - \sigma_f^*\right) \tag{21}$$

where $\sigma_i^*$ and $\sigma_f^*$ are the normalized strength of material at intact and fracture status, respectively. $D$ ($0 \le D \le 1$) denotes the *damage* of material. The actual yield strength, $\sigma_y$, is obtained by multiplying the normalized strength by the strength at Hugoniot Elastic Limit (HEL), $\sigma_{HEL}$. Mathematically this is expressed by $\sigma_y = \sigma_y^* \cdot \sigma_{HEL}$. The material is said to yield when $s \ge \sigma_y$.

It can be seen from Eq. (21) that, for an intact material within elastic range, $D$ equals zero and the normalized material strength equals $\sigma_i^*$. The *damage* in the JH2 model is a function of cumulative plastic strain. When the plastic strain reaches the maximum capacity, $D$ evolves to 1.0 and the material strength equals $\sigma_f^*$. The strength envelops at the intact and failure status are conceptually illustrated in Fig. 1. They are calculated by

$$\sigma_i^* = A(p^* + T^*)^N(1 + C \cdot ln\dot{\varepsilon}^*) \tag{22}$$

$$\sigma_f^* = B(p^*)^M(1 + C \cdot ln\dot{\varepsilon}^*) \tag{23}$$

where *A, B, C, M, N* are material constants, $p^* = p/p_{HEL}$ is the normalized pressure and $p_{HEL}$ represents the pressure at HEL. $T^* = T/p_{HEL}$ where $T$ is a material constant representing the maximum tensile hydrostatic pressure the material can withstand. For Eq. (22) to be valid, it needs to be ensured that the material does not undergo a tension failure. In other words, if the material bears a tensile hydrostatic pressure, the magnitude of the normalized pressure $p^*$ must not exceed the magnitude of the normalized tensile strength $T^*$. Otherwise, the material point will be set to fail. $\dot{\varepsilon}^* = \dot{\varepsilon}/\dot{\varepsilon}_n$ is a normalized strain rate and the normalizer, $\dot{\varepsilon}_n$, is taken as $1.0\ s^{-1}$. The equivalent strain rate, $\dot{\varepsilon}$, is calculated by

$$\dot{\varepsilon} = \sqrt{2/3 d_{ij} d_{ij}} \tag{24}$$

where $d_{ij}$ represents element in the deviatoric strain tensor.

The pressure is calculated based on the Hugoniot equation of state to represent the nonlinear response of the material. The numerical implementation uses the Taylor expansion of the Hugoniot equation of state, which is expressed by

$$p = \begin{cases} K_1\mu + K_2\mu^2 + K_3\mu^3 + \Delta p\ , & if\ \mu \ge 0 \\ K_1\mu + \Delta p, & elsewise \end{cases} \tag{25}$$

where $K_1$, $K_2$, and $K_3$ are material constants and $K_1$ equals the bulk modulus. The compression, $\mu$, is calculated by $\mu = (\rho/\rho_0) - 1$ with $\rho$ and $\rho_0$ being the current and initial density, respectively. The term $\Delta p$ represents an incremental hydrostatic pressure due to loss of internal energy. $\Delta p$ is non-zero only when the damage is greater than 0, i.e., plastic deformation has started to accumulate. Under that circumstance, $\Delta p$ is updated by

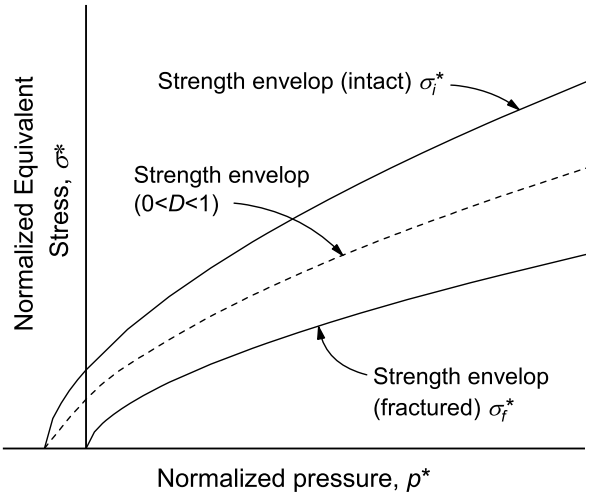


**Fig. 1.** Conceptual illustration of the strength envelopes in the JH2 model.

$$\Delta p_{t+\Delta t} = -K_1\mu_{t+\Delta t} + \sqrt{(K_1\mu_{t+\Delta t} + \Delta p_t)^2 + 2\beta K_1 \Delta U} \tag{26}$$

where $\beta$ is a factor indicating the percentage of internal energy loss that contributes to the incremental hydrostatic pressure. The loss of internal energy, $\Delta U$, is assessed by

$$\Delta U = U_t - U_{t+\Delta t} \tag{27}$$

$$U_t = \sigma^2/(6G) \tag{28}$$

where $\sigma$ represents the equivalent von Mises stress on the yield surface. After yielding, the material experiences a gradual softening with increasing plastic strain. Therefore, the magnitude of $\sigma$ is gradually reduced with the progress of damage and $\Delta U$ is therefore positive.

The damage $D$ in Eq. (21) is a function of the cumulative plastic strain as expressed by

$$D = \frac{\sum \Delta\varepsilon^p}{\varepsilon_f^p} \tag{29}$$

where $\varepsilon_f^p$ denotes the ultimate plastic strain the material can bear before fracture. It is calculated by

$$\varepsilon_f^p = D_1(p^* + T^*)^{D_2} \tag{30}$$

where $D_1$ and $D_2$ are material constants. $\Delta\varepsilon^p$ in Eq. (29) represents an incremental plastic strain. It is obtained through the following three steps.

(1) Since the material is found to have yielded, the stress calculated in Eq. (19) would be outside the yield surface. The stress is adjusted to the yield surface through a radial return algorithm which writes

$$\boldsymbol{\sigma}_y^d = (\sigma_y / s)\boldsymbol{\sigma}^d \tag{31}$$

where $\boldsymbol{\sigma}_y^d$ represents the adjusted deviatoric stress tensor. The algorithm essentially reduces all stress components by a factor so that the equivalent stress is returned to the yield surface.

(2) The plastic deviatoric strain increment is determined by subtracting the incremental elastic deviatoric strain from the total incremental strain, or expressed by

$$\Delta\boldsymbol{\varepsilon}_d^p = \Delta\boldsymbol{\varepsilon} - \Delta\boldsymbol{\varepsilon}_d^e \tag{32}$$

where $\Delta\boldsymbol{\varepsilon}$ has been obtained when implementing Eq. (19) and its elastic part, $\Delta\boldsymbol{\varepsilon}_d^e$, is linearly related to the change in stress between two consecutive time steps.

(3) The calculated $\Delta\boldsymbol{\varepsilon}_d^p$ is projected onto the stress direction by

$$\Delta\widehat{\varepsilon}_{d_{ij}}^p = \Delta\varepsilon_{d_{ij}}^p \frac{\tau_{ij}}{s} \tag{33}$$

which gives the incremental plastic strain tensor. The equivalent incremental plastic strain is then obtained by

$$\Delta\varepsilon^p = \sqrt{2/3\Delta\widehat{\varepsilon}_{d_{ij}}^p \Delta\widehat{\varepsilon}_{d_{ij}}^p} \tag{34}$$

which is used in Eq. (29) for updating the damage value.

For material points that experience plastic strain, the Cauchy stress computed in Eq. (19) is recalculated using the returned deviatoric stress and updated hydrostatic pressure:

$$\boldsymbol{\sigma}'_t = \boldsymbol{\sigma}_y^d + \boldsymbol{I}p_t \tag{35}$$

where $p_t = \sigma'_v + \Delta p_t$ is the updated magnitude of hydrostatic pressure and $\sigma'_v$ refers to the hydrostatic pressure in the predicted $\boldsymbol{\sigma}'_t$ in Eq. (19). The calculated Cauchy stress is then rotated by

$$\boldsymbol{\sigma}_t = \boldsymbol{R}_t \boldsymbol{\sigma}'_t \boldsymbol{R}_t^T \tag{36}$$

and the result is returned to the NOSB PD computational framework to calculate the peridynamic force state.

### 2.3. Tension failure model

It is well known that fracture away from the detonation location is largely attributed to tensile stress along the circumferential direction of the stress wave. Tension failure also accounts for the ring-type fractures, or spalling, observed in experiments, as a result of superposition of stress waves. Although the JH2 model can also be used to model tension failure, there are two major concerns if it is used for modelling the blasting induced fractures. First, the JH2 model does not explicitly consider the variation of tensile strength of rock with strain rate. A constant dynamic tensile strength (greater than the static tensile strength) is used in the JH2 model. In fact, higher strain rate was found to result in high tensile strength of rock and such effect appeared to be apparent with strain rate greater than a threshold at approximately 0.5 or 1 $s^{-1}$ (Cho et al., 2003). The strain rate near a blasting site is typically a lot higher than such threshold. Therefore, it is desirable to consider the variation of rock tensile strength with strain rate for better quantification of rock properties. Second, the blasting induced fracture is largely dependent of the stress direction. Nonetheless, the tensile failure is gauged in the JH2 model using a hydrostatic pressure, which is related to bulk strain and does not account for stress/strain direction. The model therefore may not be able to predict failure for cases where the material is stretched along one direction but compressed along another direction. In those cases, the material may fail under the tensile stress while the magnitude of the hydrostatic pressure remains low.

In the present study, a tensile stress-based failure model is implemented in conjunction with the JH2 model to simulate tensile fracture of rock. The model is based on a minor principal stress criterion and considers strain rate effect on the tensile strength of rock. A material point is said to fail if the minor principal stress is smaller than the dynamic tensile strength of the material. It is expressed by:

$$\sigma_3 < \sigma_{dt} \tag{37}$$

The dynamic tensile strength of the material, $\sigma_{dt}$, is described by

$$\sigma_{dt} = \begin{cases} \sigma_{st}, & \left(\dot{\varepsilon} \le \dot{\varepsilon}_0\right) \\ \exp\left[C_1 \ln\left(\dfrac{\dot{\varepsilon}}{\dot{\varepsilon}_0}\right)\right]\sigma_{st}, & \left(\dot{\varepsilon} > \dot{\varepsilon}_0\right) \end{cases} \tag{38}$$

where $\dot{\varepsilon}$ refers to the equivalent strain rate at a specific point as calculated in Eq. (24) and $\dot{\varepsilon}_0$ is a critical strain rate since where the dynamic effect is considered. The Eq. (38) essentially describes a bilinear relationship between the strain rate and tensile strength as illustrated in Fig. 2. That is, for strain rates below $\dot{\varepsilon}_0$, the tensile strength is represented by a constant static tensile strength $\sigma_{st}$; for strain rates above $\dot{\varepsilon}_0$, the tensile strength increases exponentially with the strain rate. The critical strain rate $\dot{\varepsilon}_0$ has been selected to be 0.4 $s^{-1}$ in this study. The constant $C_1$ correlates the strain rate with the dynamic tensile strength. Based on available experimental data of different rocks Cho et al., 2003), the constant is selected to be 0.33. The static tensile strength of the granite rock that will be modelled later has been determined to be −6.9 MPa (Banadaki, 2010). Note that the tensile strength in Eq. (37) and ((38) has a

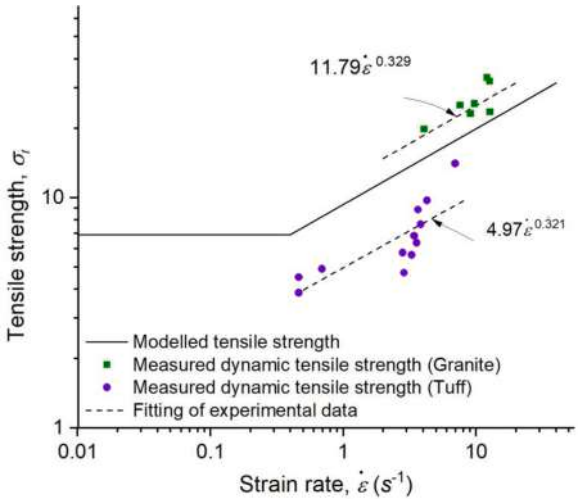


**Fig. 2.** Illustration of the bilinear relationship between strain rate and dynamic tensile strength of rock. Experimental data is extracted from Cho et al. (2003).

negative sign.

### 2.4. Point damage and bond breakage

In peridynamics, fracture is modelled by breaking the bonds between material points. The breakage of a bond can be determined with different approaches. In OSB PD, the bond breakage is often determined based on strain or strain energy density at bond level (Zhu and Zhao, 2019; Foster et al., 2011). In NOSB PD, there are many potential choices, both stress-based and strain-based criteria having been selected (Shou et al., 2019; Warren et al., 2009). In those criteria, a virtual stress/strain is computed at a bond based on the stress/strain at the connecting points. Breakage of the bond is determined by setting a critical level with respect to the stress/strain. In the present study, a slightly different approach is employed. Breakage of bonds is determined based on the condition of the related material points. As described in earlier sections, a material point is said to fail when: i) its damage reaches 1.0 in the JH2 damage model; or ii) the tensile stress exceeds the strength of the material. In the case of a material point failure, two groups of bonds will be set broken: i) all bonds that connect to the failed point; and ii) all bonds that cross the vicinity of the failed point. This is schematically illustrated in Fig. 3. Breaking the first group of bonds is natural, as the failed material point is no longer expected to interact with its neighbours in the framework of continuum mechanics. The second group of bonds are set to broken to simulate the opening of crack. As illustrated in Fig. 3, when a crack extends from the left to the right, the upper and lower portion of the material is being physically separated by the crack and the interaction between the two halves should be removed, even if a bond does not directly connect to the failed material point. Technically, we assume that if the minimum distance between a failed point and a bond is within half of the element size, the bond is considered to be within the vicinity of the point and will be set to broken. If the bonds in the vicinity of a failed point are not deactivated, the simulation may exhibit exceedingly thick crack zone which may not be realistic.

In the framework of peridynamics, damage of a material point can be expressed by a weighted percentage of broken bonds as

$$\varphi = 1 - \frac{\int_{\Omega_x} g\langle \boldsymbol{\xi} \rangle dV_{x'}}{\int_{\Omega_x} dV_{x'}} \tag{39}$$

where $\varphi$ represents damage and $g\langle \boldsymbol{\xi} \rangle$ represents status of a neighbouring bond. For an intact material point, $g\langle \boldsymbol{\xi} \rangle$ is set to 1 for all bonds and the $\varphi$ equals zero. For a failed material point, all its neighbouring bonds have $g\langle \boldsymbol{\xi} \rangle$ of zero and the damage equals 1. The damage value can be used to locate fracture surfaces such as shown in Fig. 9. Note that the damage introduced here is a concept in peridynamics which is different to the damage in the JH2 model that represents the relative amount of plastic strain. A failed material point (with $\varphi$=1) is no longer computed as part of a continuum media. However, it can still interact, as a discrete point, with other points through contact. In the present study, a bond-level contact force density (when applicable) is computed by

$$\boldsymbol{f}_c = min\left\{0,\ \frac{c_s}{\delta}\omega\langle \| \boldsymbol{\xi} \| \rangle \left( \| \boldsymbol{Y} \| - \| \boldsymbol{\xi} \| \right)\right\}(1 - g\langle \boldsymbol{\xi} \rangle)\frac{\boldsymbol{Y}}{\| \boldsymbol{Y} \|} \tag{40}$$

where $c_s$ is a stiffness defined by $18k/(\pi\delta^4)$ which follows the force density form in the BBPD. The Eq. (40) essentially computes a repulsive force between two unbonded points, only if their distance is less than the initial distance. Such repulsive force is necessary to transmit compressive pressure, particularly when a material is loaded above the HEL and consequently loses its shear strength and behaves like fluid. A drawback of implementing Eq. (40) is that it may introduce unphysical kinetic energy into the simulation after a large number of simulation steps. To keep numerical stability, a damping is applied to the damaged points during the time integration. The half-step velocity is updated by

$$\dot{\boldsymbol{u}}^{n+1/2} = \left[(2 - c\Delta t)\dot{\boldsymbol{u}}^{n-1/2} + 2\Delta t\ddot{\boldsymbol{u}}^{n}\right] \Big/ (2 + c\Delta t) \tag{41}$$

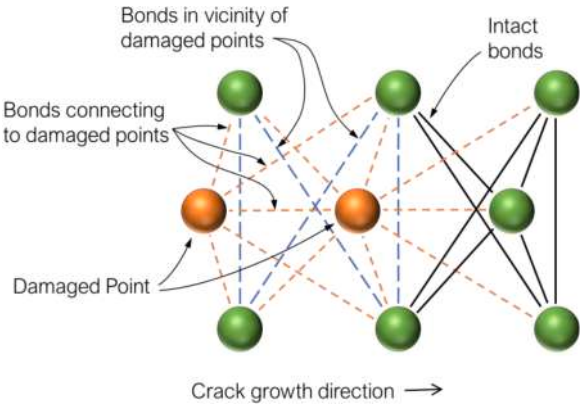


**Fig. 3.** Schematic illustration of bond breakage. The bonds in dashed lines are those set to broken based on failure at material points. For clarity, the illustration does not include all bonds at each material point.

where the damping coefficient $c$ is selected to be 0.2. The Eq. (16) and (18) are replaced with this scheme for application of damping. It should be noted that the damping only applies to the damaged material point (which has $\varphi$=1) and does not affect the formulation of the continuum material.

### 2.5. Artificial viscosity

In simulation of shock wave impact, unphysical oscillations may develop near the impact location and a relaxation term is usually needed to avoid such oscillation and maintain numerical stability (Gharehdash et al., 2020; Lai et al., 2018; Silling et al., 2017). In the present study, we implement an artificial viscosity similar to the one introduced by Silling et al. (2017) which suits the state-based peridynamics formulation. The viscosity is fundamentally similar to the viscous pressure term adopted in SPH simulations (Monaghan, 1987; Liu and Liu, 2016). It is computed by

$$\boldsymbol{T}_v = \frac{\upsilon^2}{\gamma\delta}\left(C_q\rho_0\phi^2 - C_l\rho_0 c_0\dot{\boldsymbol{Y}}\langle\boldsymbol{\xi}\rangle\cdot\boldsymbol{\xi}\Big/\parallel\boldsymbol{\xi}\parallel\right)\boldsymbol{\xi} \tag{42}$$

where $\rho_0$ and $c_0$ refer to the reference density of rock and bulk wave speed, respectively. The reference density is taken as the density of rock at initial (undeformed) configuration. $\gamma$ is a weighted volume calculated by

$$\gamma = \int_{\Omega_x}\omega\langle\parallel\boldsymbol{\xi}\parallel\rangle dV_{x'} \tag{43}$$

and $\upsilon = \rho_0/\rho$ represents relative compression, where $\rho_0$ and $\rho$ refer to the initial and current density, respectively. The current density can be obtained based on the volumetric strain at the point. The effective velocity change within the *family*, as denoted by $\phi$, is calculated by

$$\phi = \frac{1}{\gamma}\int_{\Omega_x}\omega\langle\parallel\boldsymbol{\xi}\parallel\rangle\dot{\boldsymbol{Y}}\langle\boldsymbol{\xi}\rangle\cdot\boldsymbol{\xi}\Big/\parallel\boldsymbol{\xi}\parallel dV_{x'} \tag{44}$$

The two dimensionless constants in Eq. (42), $C_q$and $C_l$, are taken to be 8.0 and 0.1, respectively, which are found to offer reasonable results after testing different combinations.

### 2.6. Modelling explosives

The explosive gas is simulated with the recently proposed updated Lagrangian formulation of peridynamics in the non-ordinary state-based form (Bergel and Li, 2016; Behzadinasab and Foster, 2020). The updated Lagrangian formulation is designed for handing problems that involve large mesh distortion. Its main feature is that the shape of the family of a material point does not change while the neighbouring points will be updated at each step. The response of the material will depend on the current deformed configuration but not the reference configuration. Correspondingly, the shape tensor is defined at the current configuration by

$$\boldsymbol{M}_x = \int_{B_x}\omega\langle\parallel\boldsymbol{Y}\parallel\rangle\boldsymbol{Y}\otimes\boldsymbol{Y}\,dV_{x'} \tag{45}$$

and the spatial velocity gradient tensor is defined by

$$\boldsymbol{L}_x = \left[\int_{B_x}\omega\langle\parallel\boldsymbol{Y}\parallel\rangle\dot{\boldsymbol{Y}}\otimes\boldsymbol{Y}\,dV_{x'}\right]\boldsymbol{M}_x^{-1} \tag{46}$$

where $B_x$ denotes the family of a material point at the deformed configuration. The trace of the spatial velocity gradient, which represents the volumetric strain rate at a point, is computed at each computation step to update the volume and density of the material point. The force state is computed by

$$\boldsymbol{T}\langle\boldsymbol{x}'-\boldsymbol{x}\rangle = \omega\langle\parallel\boldsymbol{Y}\parallel\rangle\boldsymbol{\sigma}_x\boldsymbol{M}_x^{-1}\boldsymbol{Y} \tag{47}$$

where the Cauchy stress $\boldsymbol{\sigma}_x = -p\boldsymbol{I}$ is obtained based on the pressure in the explosive gas. To allow the energy to dissipate, an artificial damping with coefficient of 0.01 is applied to the explosive gas during the step integration. The updated Lagrangian formulation of NOSB PD has been proven to be energy conservative. However, an unfavourable material instability issue has been identified (Behzadinasab and Foster, 2020) which may limit its applicability. The instability originates from the non-convexity of the energy function. Nonetheless, the model presented in this study does not appear to suffer from such instability, probably because the explosive gas is under compression only.

To model the blasting induced pressure in the high explosives, we employ the Jones–Wilkins–Lee (JWL) equation of state, in which the pressure upon detonation is described by

$$p = A\left(1-\frac{\omega}{R_1V_R}\right)\exp(-R_1V_R) + B\left(1-\frac{\omega}{R_2V_R}\right)\exp(-R_2V_R) + \frac{\omega e_0}{V_R} \tag{48}$$

where $A$, $B$, $R_1$, $R_2$, and $\omega$ are material constants, $e_0$ is the specific internal energy and $V_R$ is the ratio of initial density $\rho_0$ and current density $\rho$ of the explosive material.

In the blasting test that will be simulated later, a copper tube is inserted into the drillhole to prevent the explosive gas penetrating into the blasting-induced fractures in rock. The tube is explicitly modelled and is set to interact with both the explosive gas and the rock. Interaction of the three materials is schematically illustrated in Fig. 4. Family of material points of the explosives includes the copper so that the pressure generated within the explosives are passed to the copper. The material points in the copper tube and the rock are bonded within each other's horizons. No bond is established directly between the explosives and the rock in view of the fact that the blasting load is transferred onto the rock through the copper tube. Since the volume of the explosives and copper tube is much smaller than the size of the rock sample, a finer discretization is used, resulting in different horizons between the different materials. The dual-horizon formulation (Ren et al., 2016 & 2017) has been employed to compute the bond forces where different materials interact.

### 2.7. Numerical implementation

The numerical implementation of the formulations presented in Section 2.1 through 2.6 is summarised into the following steps and a computational chart is provided in Fig. 5.

1) At each time step, update velocity and position of material points following Eqs. (16), (17) and (41);
2) Compute detonating pressure in the explosive gas following Section 2.6;
3) Go through the steps outlined in Section 2.1 to compute unrotated rate of deformation tensor at each point of the rock (that has not been fully damaged) and the copper tube;
4) Assume a linear elastic material response, compute the trial Cauchy stress tensor following Eq. (19) and the equivalent shear stress following Eq. (20). Compute normalized strain rate, compression $\mu$, and normalized pressure $p^*$;
5) Determine if the material fails under tension by comparing normalized pressure, $p^*$, with the normalized hydrostatic tensile strength, $T^*$. In case of tensile failure, go to Step 8;
6) Compute intact and fracture strengths using Eq. (22) and (23) and the yield strength using Eq. (21). Compare the equivalent stress calculated in Step 4) with the yield strength. If the material does not yield, go to Step 8.
7) If yielding occurs, update damage in the JH2 model using Eq. (29) and compute Cauchy stress tensor following Eq. (35);
8) Following the formulations in Section 2.1 to compute the force density at each bond, including Hourglass correction term and contact force density term when applicable;
9) Compute artificial viscous force density term described in Section 2.5;
10) Update the velocity for a half step following Eq. (18);
11) Check tensile failure of material following Eqs. (37) and (38);
12) Find all points that fail in the JH2 model and the tension failure model. Set bond breakage following Section 2.4;
13) Repeat the computation loop from Step 1.

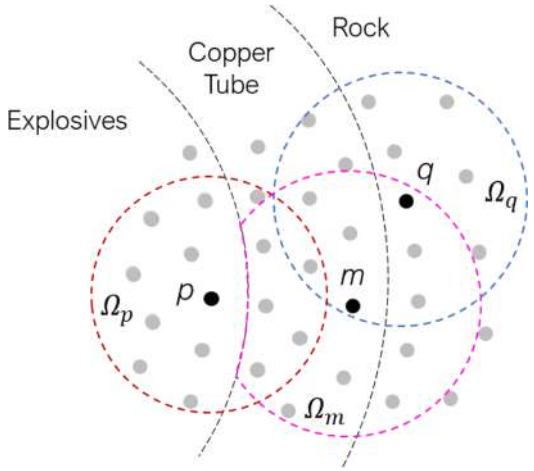


**Fig. 4.** Schematic illustration of the modelling of interactions between explosives, copper tube, and rock.

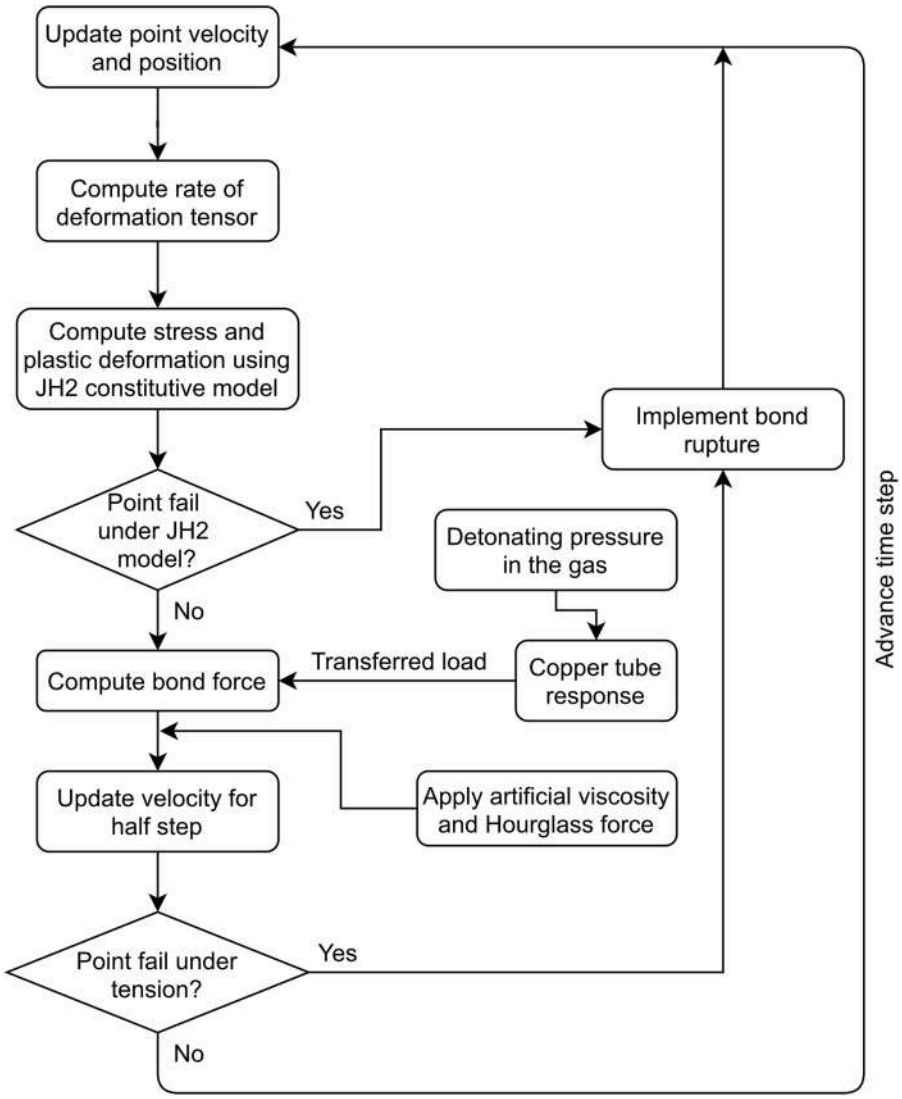


**Fig. 5.** Computational flow chart for modelling blasting induced rock fractures.

## 3. Simulation of a single-hole blasting

### *3.1. Model setup and parameter selection*

The formulations and algorithms described in Section 2 are employed to simulate single-hole blasting of granite rock following the experimental settings in Banadaki (2010). The numerical model is developed with a goal to replicate the experimentally observed blasting induced fractures. The simulated rock specimen has the same cross-sectional geometry as in the experiment. As shown in Fig. 6, the simulated sample is a 50 mm thick cylinder with diameter of 144 mm and a borehole of 6.4 mm diameter. The copper tube is 0.6 mm thick and is located immediately inside the borehole. The explosives are placed inside the copper tube. The discretisation uses an element size of approximately 0.8 mm, 0.3 mm and 0.4 mm for the rock, copper tube, and explosives, respectively, leading to a total of 1,654,208 material points. The horizons used for the three materials are 2.4 mm, 1.0 mm and 1.5 mm, respectively. The studied rock has a density of 2660 kg/m$^3$ with a shear modulus of 25.7 GPa and a bulk modulus of 21.9 GPa as reported in experiments (Banadaki, 2010). The static tensile strength of the rock was measured to be 6.9 MPa.

Applying the JH2 model requires a comprehensive set of material parameters. The selected parameters for the granite rock are summarised in Table 1. Generally, the parameters can be classified into three groups – the equation of state, the strength model and the damage model. The intact strength parameters are calibrated with uniaxial compressive strength of the rock. That is, the strength obtained from Eq. (22) with the strain rate term set to unity is set to equal the uniaxial compressive strength (161 MPa) measured in experiment (Banadaki and Mohanty, 2012). The strength at HEL ($\sigma_{\mathrm{HEL}}$) is calculated by 3/2($HEL$-$p_{\mathrm{HEL}}$) which equals 1.2 GPa. The rest

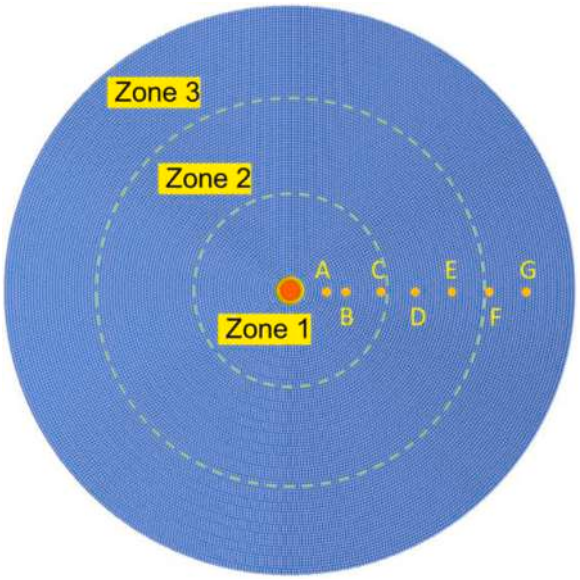


**Fig. 6.** Peridynamic model setup. The model consists of three materials: the explosives at the centre, the copper tube surrounding the explosives, and the rock material outside the copper tube. Points A to G are selected for the subsequent analysis. Zone 1 to Zone 3 within the rock material are designated for assessing crack density.

**Table 1**
Parameter selection for the JH2 model.

| Parameter | | Adopted | Values used in literatures |
|---|---|---|---|
| *Equation of state* | | | |
| Polynomial constant | $K_2$ (GPa) | –4500 | –23 ~ –4,500 (granite); –23 (sandstone); 700 (dolomite) |
| Polynomial constant | $K_3$ (GPa) | 300,000 | 2,485~300,000 (granite); 2,980 (sandstone); 5,650 (dolomite) |
| *Strength model* | | | |
| Hugoniot elastic limit | *HEL* (GPa) | 4.5 | |
| Pressure at HEL | $p_{\mathrm{HEL}}$ (GPa) | 3.7 | |
| Intact strength constant | *A* | 1.9 | 0.76~3.32 (granite); 1.01 (sandstone); 0.78 (dolomite) |
| Intact strength exponent | *N* | 0.62 | 0.62~0.84 (granite); 0.83 (sandstone); 0.45 (dolomite) |
| Fracture strength constant | *B* | 0.25 | 0.25~1.0 (granite); 0.68 (sandstone); 0.65 (dolomite) |
| Fracture strength exponent | *M* | 0.62 | 0.60~0.83 (granite); 0.83 (sandstone); 0.45 (dolomite) |
| Strain rate coefficient | *C* | 0.005 | 0.005 (granite, sandstone) |
| Tensile capacity | *T* (MPa) | 54 | 53~150 (granite); 45 (sandstone); 29 (dolomite) |
| *Damage model* | | | |
| Energy conversion ratio | $\beta$ | 0.5 | 0.5~1.0 |
| Damage constant | $D_1$ | 0.005 | 0.005~0.4 (granite); 0.005 (sandstone); 0.001 (dolomite) |
| Damage constant | $D_2$ | 0.7 | 0.435~1.0 (granite); 0.7 (sandstone); 1.15 (dolomite) |

parameters are selected following Banadaki (2010) in which the JH2 parameters were calibrated with FEM based numerical studies and by comparing with experimental data. To gain further confidence on the chosen parameters, a literature review on the JH2 model parameters used for rock in past studies (Banadaki and Mohanty, 2012; Banadaki, 2010; Wang et al., 2018; Yi et al., 2017; Ma and An, 2008; Xie et al., 2019; Gharehdash et al., 2020; Baranowski et al., 2020) is included in the table for reference. The adopted parameters largely fall within the typical range for granite rocks.

The blasting load is modelled following the formulations described in Section 2.6. The parameters used for the JWL equation of state, which follows Banadaki and Mohanty (2012), are summarised in Table 2. By applying the JWL equation of state, a detonation pressure up to 1,800 MPa is generated within the explosives which propagates at the velocity of detonation (VOD) of 6,690 m/s (Banadaki and Mohanty, 2012). The pressure level is comparable to earlier studies (Banadaki, 2010; Banadaki and Mohanty, 2012) which projected a peak pressure of 1,600 MPa at the borehole wall. The modelled detonating pressure and its propagation are

**Table 2**
Parameters used in the JWL equation of state.

| Parameter | Density | A | B | $R_1$ | $R_2$ | ω | $e_0$ |
|---|---|---|---|---|---|---|---|
| Unit | kg/m$^3$ | GPa | GPa | – | – | – | kJ/m$^3$ |
| Value | 1,320 | 568 | 21.6 | 5.81 | 1.77 | 0.282 | 7.38×10$^6$ |

exhibited in Fig. 7. The blasting induced wave and its propagation in the rock mass are presented in Fig. 8. The series of stress waves along both radial and thickness directions can be well captured. The copper tube is simulated as an elastic-plastic material with an assumed yield stress of 450 MPa. The yield stress is an estimation based on the Johnson-Cook material model which considers the strain rate effect and temperature effect (Gharehdash et al., 2020). The copper is modelled with a density of 8,960 kg/m$^3$, a bulk modulus of 130 GPa and a shear modulus of 45 GPa. It should be noted that the main role of the simulated copper tube here is to pass the blasting load onto the rock and we have not specifically applied an equation of state for the copper. A more precise way to model the detonation process is perhaps to explicitly simulate all materials loaded in the borehole, such as the explosives, coupling media, polyethylene sheath, and the copper tube (Wang et al., 2018; Gharehdash et al., 2020). This is beyond the scope of the present study. The blasting load may also be modelled in simplified ways, for example, by applying a boundary condition on the inner boundary of the rock in the form of an initial velocity, or a force density if the detonating pressure on the borehole wall is known. It is worth mentioning that the detonating pressure on the borehole may be approximated by a general pulse function (Ma and An, 2008; Baranowski et al., 2020). The time step in the simulation is selected to be 0.02 μs which is approximately one order smaller than the critical time step estimated using the approach proposed by Silling and Askari (2005). The simulation is performed to 60 μs after detonation when the major cracks cease to grow. The total simulation time is about 5 h using Intel Xeon® 4214 CPU @ 2.20 GHz with 24 cores.

### 3.2. *Fracture pattern*

Fig. 9(a-e) shows the progress of fracturing induced by the blasting as obtained in the simulation. By comparison, the fracture pattern of the rock specimen in experiments is shown in Fig. 10. Damage is first observed surrounding the borehole as all points within a zone of approximately one radius of the borehole are damaged. Radial cracks are then initiated and grow. A few major cracks continue to grow throughout the simulation, whereas others are arrested not far from the borehole. At the end of the simulation, six major radial cracks are found to extend to the outer boundary of the specimen. Minor cracks are developed in both the radial and the circumferential directions, possibly due to superposition of stress waves that travel inside the rock mass. The simulation is shown to qualitatively capture the major features of blasting induced fractures observed in the experiments, including the major cracks that split the specimen and small cracks along both the circumferential and radial directions. The dense micro cracks which was evident in the experiment are not exhaustively captured. To capture those cracks, it would probably be necessary to consider the existing micro cracks in the rock material (Zhu and Zhao, 2020). Interior view of the crack propagation is shown in Fig. 9(f-i). In Fig. 9(f), when the detonation is just initiated, damage is seen surrounding the borehole and radial cracks can already be seen on the side of detonation. Those radial cracks propagate to the other end of the sample in a nearly planar manner. However, not all the cracks propagate cross the thickness of the sample. Some radial cracks are found only on the side where the detonation starts. There also appear to be more

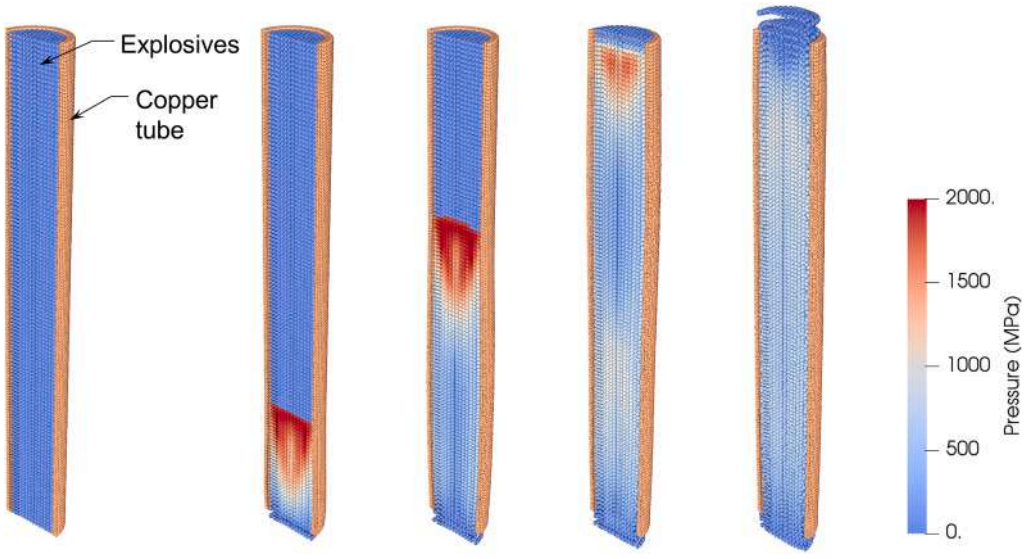


**Fig. 7.** The pressure in the explosive gas after detonation. The detonation starts at the bottom and propagates upwards. Fig. (a) shows the condition before detonation, and (b) to (e) show simulated explosive gas pressures at 2 μs, 5 μs, 8 μs, and 12 μs after detonation, respectively.

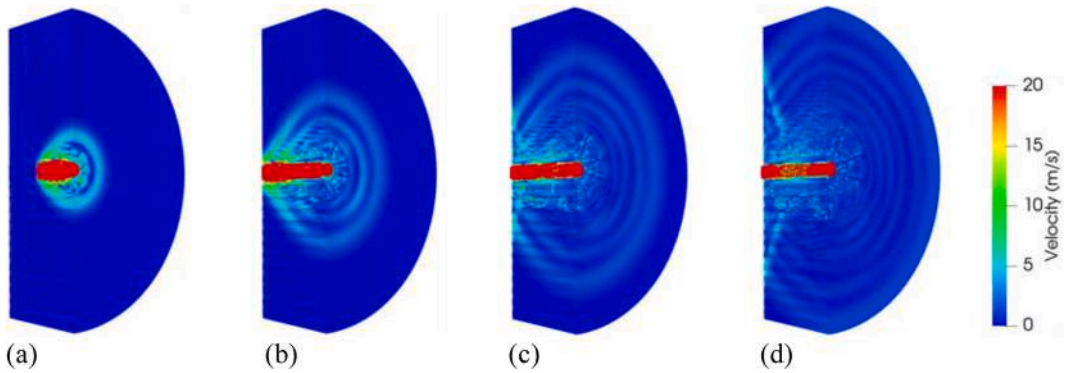


**Fig. 8.** The blasting induced wave propagation in the rock mass. Results are shown with a cross section cutting the rock sample into two halvies. (a) to (d) shows the point velocity at 4 μs, 8 μs, 14 μs and 20 μs after detonation, respectively.

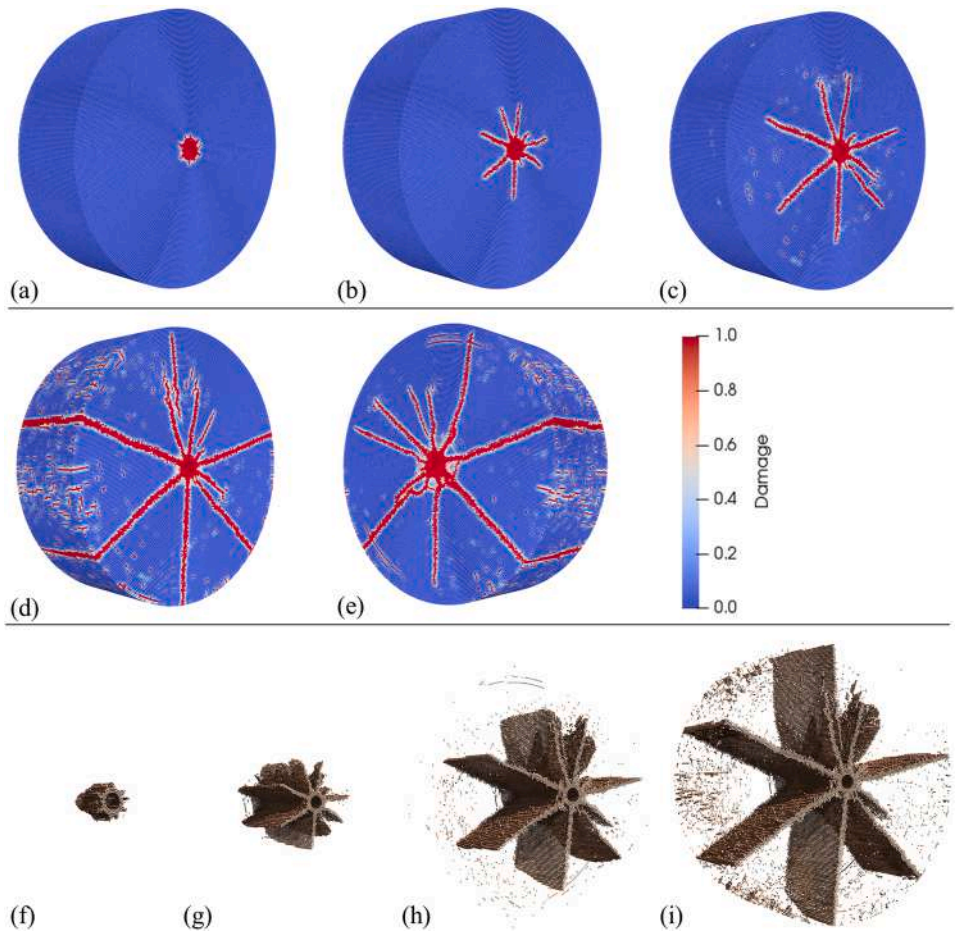


**Fig. 9.** Simulated fracture process of rock subject to single-hole blasting: (a) through (d) show exterior view of fractures at 4 μs, 20 μs, 40 μs and 60 μs, respectively. The view is from the side where detonation starts; (e) shows fractures at 60 μs from the other side of the sample; (h) through (i) exhibit interior view of fractured material points at 4 μs, 20 μs, 40 μs and 60 μs, respectively.

circumferential cracks on the far end of the detonation as indicated in Fig. 9(e). In Fig. 11, different sections are cut through the sample to examine the fracture pattern along the thickness direction. Indeed, the fracture pattern is non-uniform but the variation does not seen to be significant, although it appears that more radial cracks are generated near two ends of the sample.

The intensity of fractures can be quantitatively assessed using the concept of crack density, defined by the length of cracks per unit area. In the reported experiment, the crack density for the studied rock was measured using combined dye impregnation and digital

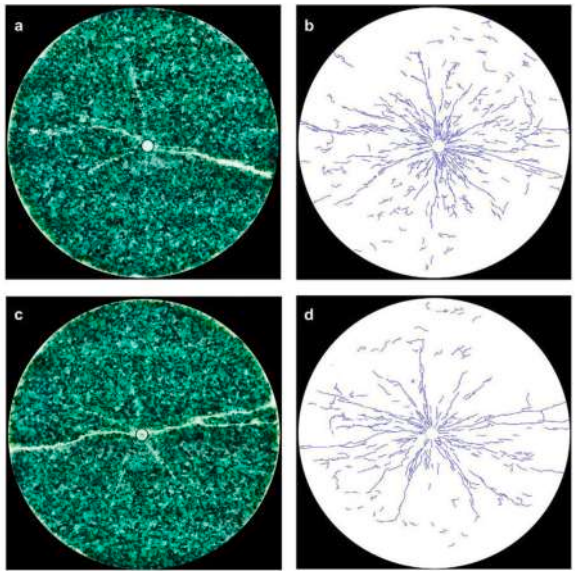


**Fig. 10.** Fracture pattern observed in experiment (Banadaki and Mohanty, 2012).

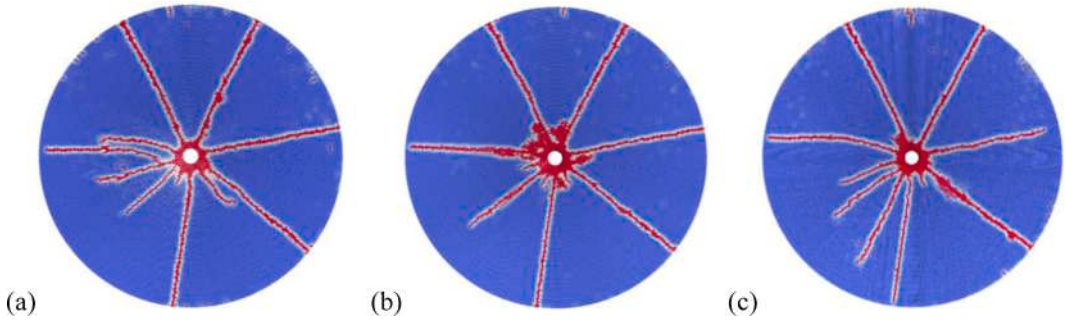


**Fig. 11.** Fracture patterns at cross sections along the thickness direction: (a) at 5 mm from detonation point; (b) at middle of the sample; (c) at 45 mm from of the detonation point.

photography techniques (Banadaki, 2010). For the purpose of analysis, the rock specimen is divided into three ring-shape zones with equal thickness as illustrated in Fig. 6. Zone 1 is where the densely situated fractures initiate and spread due to blasting. Zone 2 and 3 involve propagation and arresting of cracks as well as spalling cracks. The crack density is found to be the highest in Zone 1 which is adjacent to the blasting hole, and the lowest in Zone 3 which is near the outer boundary of the specimen. The range of crack density is found to be 0.3 to 0.46 mm/mm$^2$ in Zone 1, 0.1 to 0.18 mm/mm$^2$ in Zone 2, and 0.05 to 0.13 mm/mm$^2$ in Zone 3. In the simulation, the fracture is represented by the damage of material points (i.e., with damage equal to one). In the discretisation of the model, each material point represents a cubic area with an edge length of 0.8 mm. Therefore, we assume that each damaged material point represents a crack length of 0.8 mm and the total length of cracks within a cross section is calculated by counting the total number of damaged points. For a selected cross section, the crack density is calculated as the total length of cracks divided by the total area of the section. We have selected three cross sections along the thickness direction – two at the two ends and one in the middle – for the assessment of crack density. The crack densities obtained from the simulation are plotted in Fig. 12 in comparison with the experimentally measured data. The simulation results are comparable to the experimental measurements but generally exhibit slightly lower crack density. This difference may be attributed to the existence of micro defects in the granite which can possibly facilitate formation of densely spaced short cracks under the shock load. Such physics is not considered in the numerical model and may be incorporated by introducing pre-existing damage in the rock material. However, a finer discretisation is likely needed if one wishes to quantify those micro defects, which likely creates higher computational cost.

### *3.3. Failure mechanisms*

In the simulation, there are three mechanisms that lead to the failure of material points. In the JH2 model, a material point may fail either in tensile mode, or as a result of excessive plastic strain. In the tension damage model, a material point is damaged when the

maximum tensile stress exceeds the capacity. The mode of failure for the damaged material points is reviewed in Fig. 13. The material surrounding the borehole is found mostly damaged under the JH2 model condition due to excessive plastic strain. The radial cracks are formed under both the tensile failure mode in the JH2 model and the tension damage model. Those minor cracks on both circumferential and radial directions are formed under the tension damage model.

Material failure under the JH2 model is dependant of pressure and strain rate. We further illustrate the evolution of pressure, strain rate, material strength, and equivalent von Mises stress in the simulated rock sample in Fig. 14. The quantities are plotted at a representative cross section cutting through the middle of the sample. The time in Fig. 14 refers to the time after detonation. At 4.0 μs, the maximum hydrostatic pressure surrounding the drillhole is found to be over 80 MPa with a strain rate on the order of $1 \times 10^4\ s^{-1}$. Accordingly, the material strength near the drillhole rises to about 300 MPa which is almost twice of that in the region far from the drillhole, which allows the material to sustain higher shear stress. At the same time, the shear stress surrounding the drillhole has risen to around 200 MPa. The shear stress continues to rise and the material points immediately adjacent to the drillhole are found to be damaged at 6.0 μs. The propagation of the stress wave can be easily identified. At 12.0 μs, the magnitude of pressure at the wave front reduces to less than 20 MPa and the strain rate drops to less than 2000 $s^{-1}$. The effect of pressure and strain rate on the material strength is largely mitigated. The material strength at the wave front is around 200 MPa which is about 30% higher than that in other area. The shear stress at the wave front is mostly below 100 MPa, which is far less than the material strength. Therefore, the material mostly stays in the elastic state and plastic strain is no longer the main failure mechanism. In other words, the stress wave at this stage has been weakened and is unable to cause excessive plastic strain in the material. The main factor that triggers material failure at this stage is the tensile stress. The propagation of the cracks is found slower than the propagation of the longitudinal stress wave. This can be easily observed in the plots for the material strength, where the failed material points possess a strength of zero (as indicated in blue colour). The observation is consistent with past experimental and numerical studies where crack propagation speed was found to be lower than longitudinal wave speed (Cho and Kaneko, 2004; Daehnke et al., 1997; Sundaram and Tippur, 2018).

To further illustrate the failure mode, three points named P1 through P3 are selected along the radial direction (as indicated in Fig. 15) at a distance of 0.8 mm, 1.6 mm and 4.8 mm from the borehole wall, respectively. The hydrostatic pressure, the von Mises

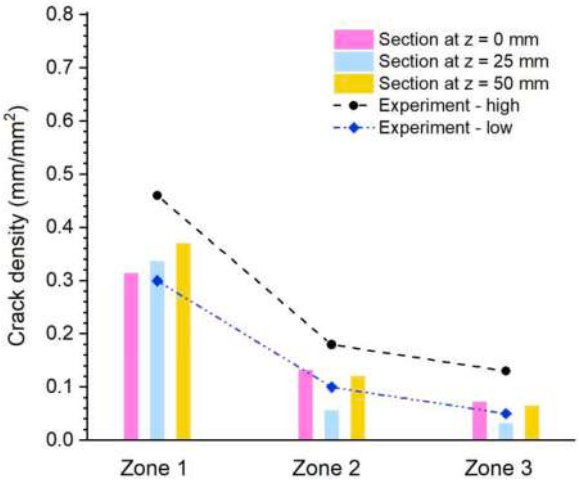


**Fig. 12.** Comparison of simulated and measured crack densities. The experimental data is obtained from Banadaki (2010).

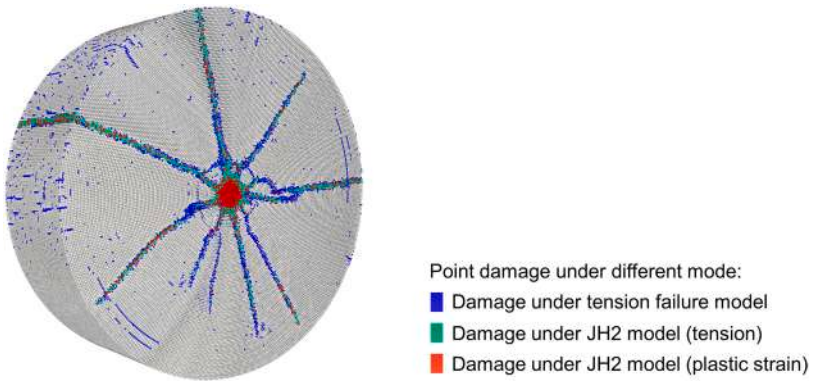


**Fig. 13.** Failure mode of the rock. The view is from the opposite side of detonation.

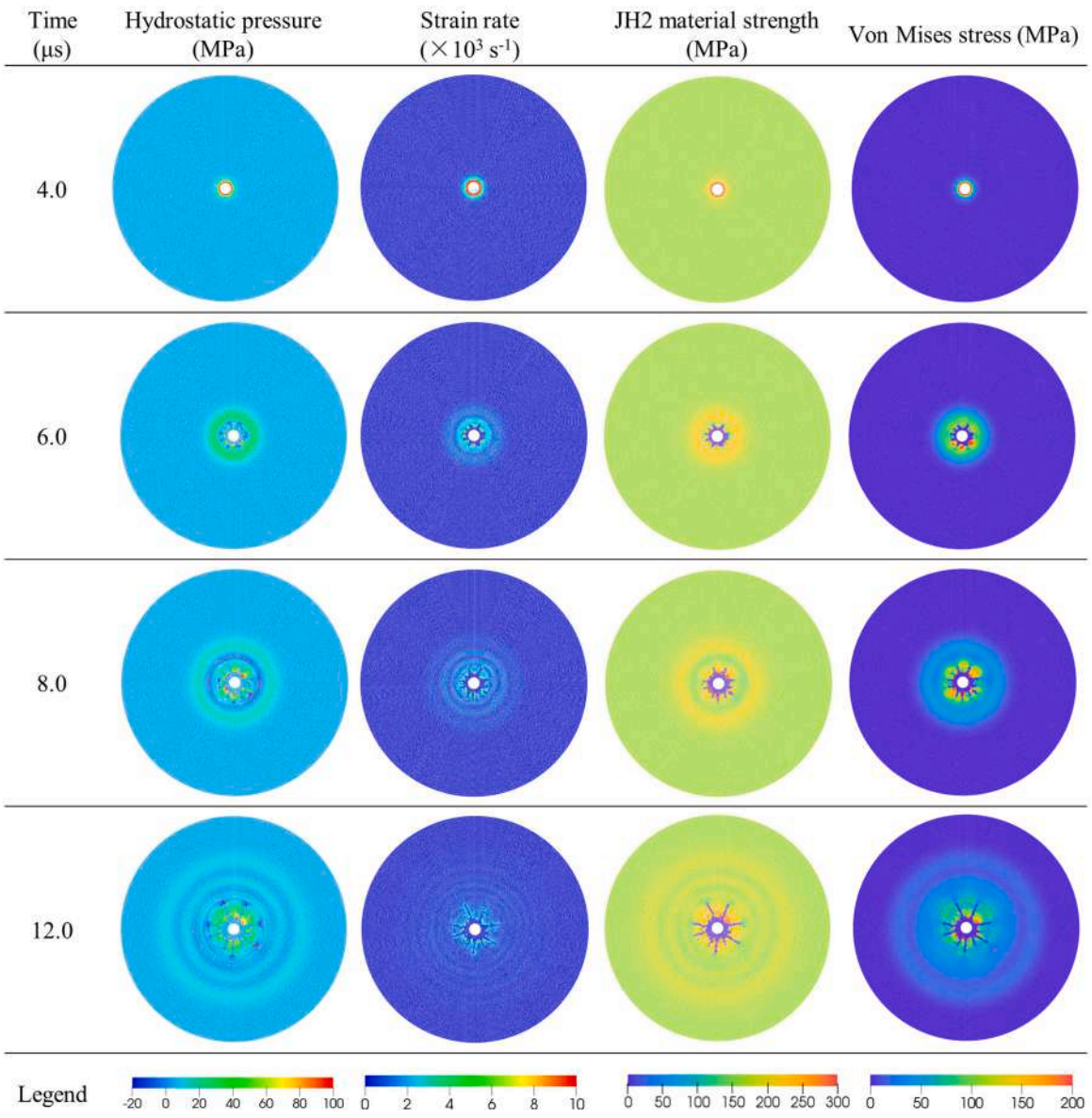


**Fig. 14.** The hydrostatic pressure, strain rate, JH2 material strength and equivalent shear stress in the simulated rock sample shortly after blasting. The section is taken crossing the centre of the sample.

stress, and the strength under the JH2 model are plotted altogether in Fig. 15. The pressure-stress path of point P1 is a typical failure path in the JH2 model. Upon detonation, the equivalent stress at the point drastically rises with increasing pressure. The stress hits the yield strength at a pressure about 200 MPa and the yield strength is almost three times of that without pressure and strain rate effects. A softening curve is followed until the point reaches its fracture. Plastic strain is accumulated after yielding. At Point P2, the pressure is much lower than that at P1, and so as the strength. The point is found yielded at a shear stress about 150 MPa followed by a flatter softening curve comparing with P1. At Point P3, which is further away from the detonation, the equivalent stress is found never reaching its strength envelope and plastic strain is no longer accumulated.

A series of points are selected along the radial direction of the simulated rock specimen on the detonation side to examine the blasting induced radial pressures. A total of seven points, namely A through G, at a distance of 6.8 mm, 10.8 mm, 22 mm, 29.2 mm, 39.6 mm, 50 mm, and 59.6 mm from the borehole wall, respectively, are selected as shown in Fig. 6. The radial stresses at those points recorded in the simulation are plotted in Fig. 16(a). Stress attenuation can be clearly observed. At Point A, the stress peaked at about 130 MPa while at point G, which is about 53 mm away, the peak stress drops to below 20 MPa. The detonation does not generate a single wave but a series of stress waves with reducing magnitude. The shape of the wave also exhibits dispersion during the propagation as indicated by the gradually widening of the front wave. Wave dispersion is known to be a feature of the SBPD owning to its non-local nature. Such feature allows the SBPD to naturally capture the wave dispersion in heterogeneous materials such as rocks (Butt

et al., 2017). We have also examined the propagation speed of the stress wave as illustrated in Fig. 16(b). The arrival time of the peak stress is recorded at each of the points and is plotted against the distance to the borehole wall. The slope of the linear fitting line therefore represents the wave speed. It is found to be about 4,270 m/s, which is within 5% difference to the measured P wave velocity of 4,535 m/s (Banadaki, 2010).

A quantitative comparison of the results with experimental data is offered in Fig. 17 with respect to the recorded peak radial stress at various distances from the borehole wall. The simulation results indicate a linear relationship between the distance to the borehole wall and the peak radial stress when plotted in the log-log space. Therefore, the peak radial stress may be expressed as a power function of the distance to the borehole wall as $p = Cd^{-n}$ where $C$ is a constant that depends on the magnitude of load. The power $n$ is found to be 0.798 in this study. The peak radial stress obtained at various distances away from the borehole is seen to agree with experimental record (Banadaki, 2010).

We further examine the PPV obtained from the simulation at varies distances from the borehole. The PPV is a quantity that has been extensively used in engineering practice to assess the extent of blasting induced damage. Holmberg and Persson (1978) proposed that the PPV is a function of the distance to the blasting hole which can be expressed by $PPV \propto Cd^{-\beta}$ where $C$ and $\beta$ are constants related to specific site conditions and explosives. Such relationship was subsequently confirmed through field measurements (Tesarik et al., 2011; Lee et al., 2018). The relationship between the PPV and the distance to blasting obtained from the simulation is examined in Fig. 18. The peak radial velocity at the seven selected points as shown in Fig. 6 are extracted and plotted. Clearly, the PPV can be well described with a power law relation in the same form that was proposed by Holmberg and Persson. The PPV is often correlated with the level of damage in the rock through empirical studies. For example, a PPV above about 400 m/s ~ 800 m/s is generally considered to cause strong radial or tensile cracks in rock and a PPV above 1500 m/s ~ 2500 m/s is believed to induce heavy damage or complete break-up of rock material (Bauer and Calder, 1978; Mojitabai and Beatie, 1996). In our simulation, the obtained PPV is well above the threshold for radial and tensile cracks. The PPV is above 2500 m/s within a distance of about 20 mm from the borehole. Indeed, significant fracturing is observed in that region (refer to Fig. 9) and major radial cracks are seen throughout the rest part of the sample.

### 3.4. Influence of discretisation

In the simulation presented above, the element size (which we denote as $\Delta x$) of the rock is selected to be 0.8 mm which is on the same order of the particles (e.g., quartz particles) with a belief that this will lead to reasonable crack density and wave dispersion. The simulation can be computationally overwhelming for a larger scale analysis. In this section, we assess the influence of different discretisation schemes on the predicted fracture pattern and pressures in rock. Four sensitivity analyses are performed with different $\Delta x$. The first and the second model are discretised with $\Delta x = 1.0$ mm and $\Delta x = 1.2$ mm, respectively. This leads to a total number of material points up to 843,609 and 515,105, respectively, for the two models. The third model uses $\Delta x = 0.7$ mm and a total of 2,400,354 material points. The last model uses adaptive meshing, where the element size is selected to be 0.8 mm near the borehole and gradually increased on the radial direction until 1.2 mm. The total number of material points is 615,609 with the adaptive meshing. The horizon at each material point is selected to be $3\Delta x$ and the dual-horizon peridynamic theory (Ren et al., 2016 & 2017) is employed for this model.

The obtained fracture patterns in the four sensitivity analyses are presented in Fig. 19. All models are found to capture the fragmentation of rock near the borehole and the major radial cracks that extend to the boundary of the sample. The difference in the fracture pattern mainly lies in the minor cracks. With larger elements there appears to be more minor cracks generated near the boundary. Formation of those minor cracks indicates stronger stress waves travelling inside the material domain. We further review the total energy (i.e., strain energy plus kinetic energy) of the rock in the four simulations as shown in Fig. 20. Upon detonation, the energy in rock rises quickly due to the high pressure in the explosive gas. When the detonation has crossed the thickness of the sample, the increase of energy in rock becomes much slower and the main physical source of energy influx is the remaining pressure in the explosives. Note there is an artificial damping implemented for the gas which dissipates part of the energy, so the energy in explosives is not expected to be fully transferred to the rock. Models with coarser discretisation tend to bear more energy, probably due to the larger horizons used which allow the blasting load to affect a greater extent. The increment in the total energy of rock is mitigated with time. With implementation of the artificial viscosity, the energy is expected to be dissipated if time is long enough. However, it appears that the energy continues to gain when coarse discretisation is used. The gaining in energy is likely numerical which originates from the contact modelling between damaged material points and intact material. This could potentially lead to unstable simulation and stronger energy dissipation may be needed for the computation. It is interesting to note that the energy evolution is rather smooth for the model with adaptive meshing under a dual-horizon peridynamics formulation while its computational cost is the second lowest. We also examine the radial pressures in the rock as presented in Fig. 21 which shows all the models give results comparable to experimental record.

### 3.5. Influence of material parameters

The presented computational approach involves a substantial number of parameters to quantify the complex physical process resulted from blasting. As such, it is essential to further examine the sensitivity of the simulation results with different modelling parameters. A sensitivity study consisting of six cases is carried out by adjusting the model parameters and assessing their influence on the fracture pattern. The investigated parameters are summarised in Table 3. Parameters not listed in the table are the same as those shown in Table 1. In the first two cases, the intact strength and fracture strength parameters in the JH2 model are adjusted to the middle range of typical granite rock parameters. In Case 3 the strain rate coefficient in the JH2 model is doubled to 0.01. In Case 4, the

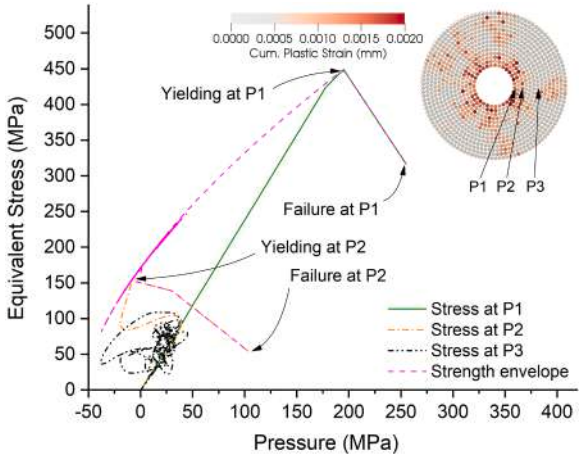


**Fig. 15.** The pressure – stress relation of selected points. Points P1 to P3 are located at 0.8 mm, 1.6 mm and 4.8 mm from the borehole wall, respectively.

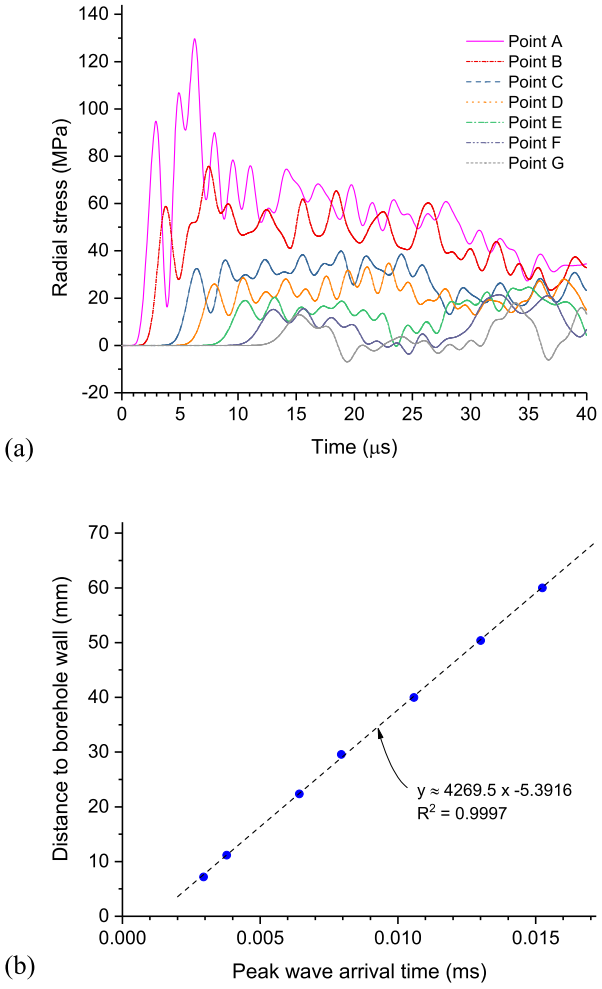


**Fig. 16.** (a) Peak radial stress at various points. Location of the points A to G are shown in Fig. 6. (b) Projected wave propagation speed based on the peak wave arrival time at points A to G.

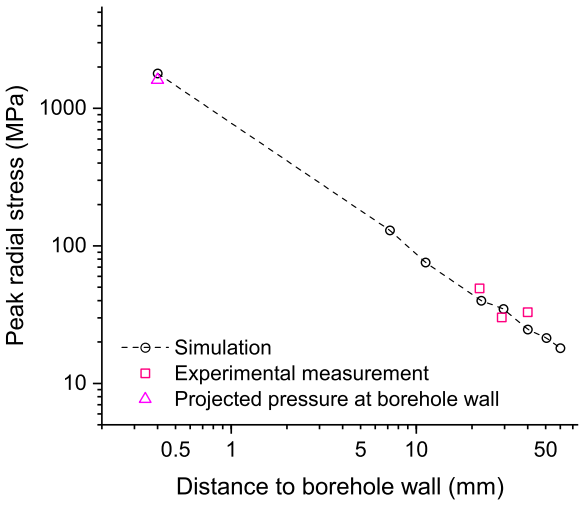


**Fig. 17.** Relationship between peak radial stress and distance to the borehole wall.

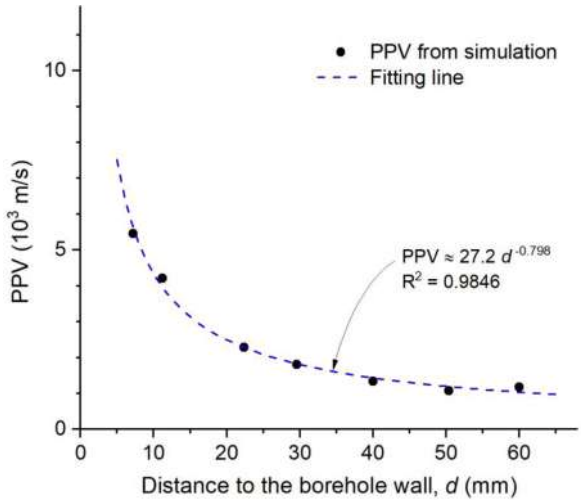


**Fig. 18.** PPV of material points at varies distances from the borehole.

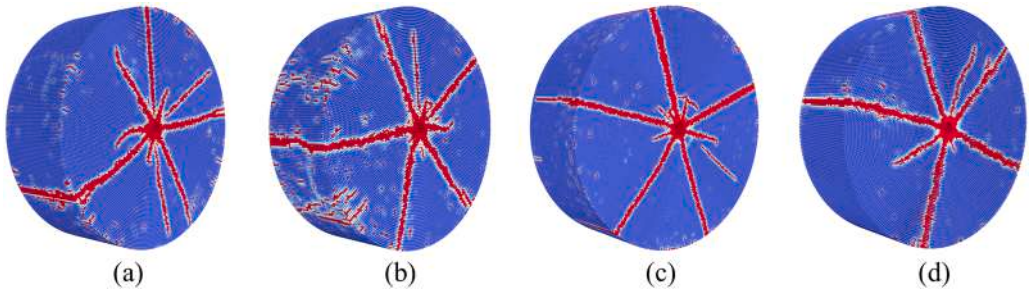


**Fig. 19.** Fracture patterns in the four sensitivity analyses with different discretisation schemes. (a) Δx = 1.0 mm; (b) Δx = 1.2 mm; (c) Δx = 0.7 mm; (d) Adaptive meshing with Δx ranging from 0.8 to 1.2 mm. View is from the detonation side.

second and third polynomial constants $K_2$ and $K_3$ in the JH2 model are set to zero, therefore neglecting the high order terms in the equation of state. In the last two cases, the critical strain rate $\dot{\varepsilon}_0$ in the tension damage model is set to 1 $s^{-1}$ and 0.1 $s^{-1}$, respectively.

The predicted fracture pattern in the six cases are shown in Fig. 22. The first four cases do not show fundamental difference in fracture pattern when comparing with the original analysis. Nonetheless, the first case appears to show less micro-cracks. In this case, a

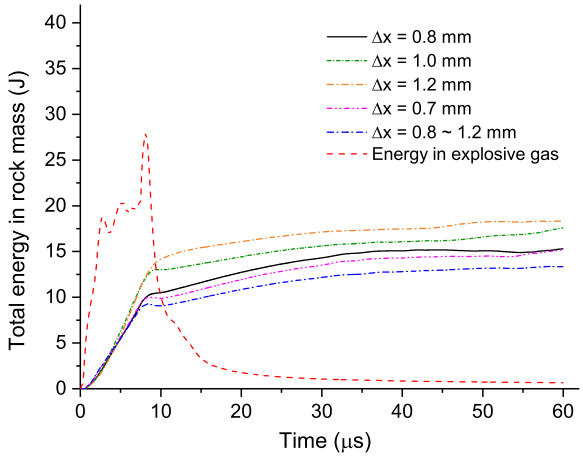


**Fig. 20.** Total energy in the simulated rock sample with different discretisation schemes.

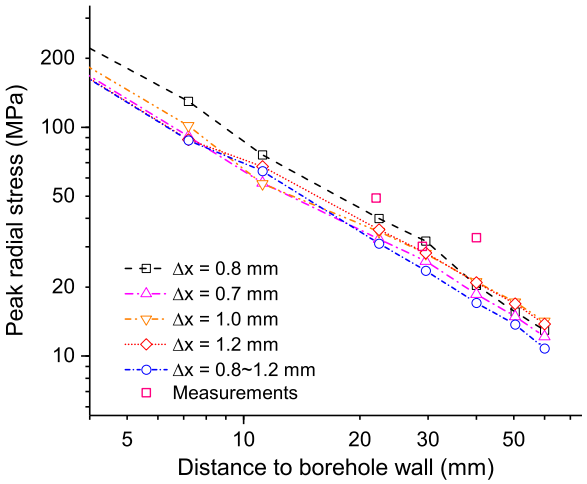


**Fig. 21.** Obtained peak radial pressure in the simulated rock sample with different discretisation schemes.

**Table 3**
Parameters in the sensitivity analyses.

| Case | N | B | M | C | $K_2$ (GPa) | $K_3$ (GPa) | $\dot{\varepsilon}_0(s^{-1})$ |
|---|---|---|---|---|---|---|---|
| 1 | 0.72 | 0.25 | 0.62 | 0.005 | −4500 | 300,000 | 0.5 |
| 2 | 0.62 | 0.5 | 0.7 | 0.005 | −4500 | 300,000 | 0.5 |
| 3 | 0.62 | 0.25 | 0.62 | 0.01 | −4500 | 300,000 | 0.5 |
| 4 | 0.62 | 0.25 | 0.62 | 0.005 | 0 | 0 | 0.5 |
| 5 | 0.62 | 0.25 | 0.62 | 0.005 | −4500 | 300,000 | 1.0 |
| 6 | 0.62 | 0.25 | 0.62 | 0.005 | −4500 | 300,000 | 0.1 |

higher intact strength exponent in Eq. (22) is used which leads to a lower intact strength in the JH2 model because the normalized pressure and tensile strength is less than 1.0. Consequently, the material is expected to fail at a lower pressure so that the magnitude of the stress wave may be mitigated and less tensile cracks would form. The results shown in Fig. 22(b-d) suggest that the fracture strength parameters and the strain rate coefficient in the JH2 model do not have apparent influence on the fracture pattern as long as they are chosen within the typical range of the material being studied. The high order terms in the equation of state are also found to have minimal influence. They may simply be taken as zero if they cannot be determined with confidence. The parameter in the tension damage model, nonetheless, appears to have remarked impact on the fracture pattern. In Case 5, where the critical strain rate is increased to 1 $s^{-1}$, the tensile strength of the material under dynamic loads is generally reduced. More radial cracks are formed. Some small ring cracks (spalling) are also observed, which can be attributed to the superposition of an outward stress wave and a reflected, inward stress wave. In Case 6, where the dynamic tensile strength of the material is increased, apparently less micro-cracks are

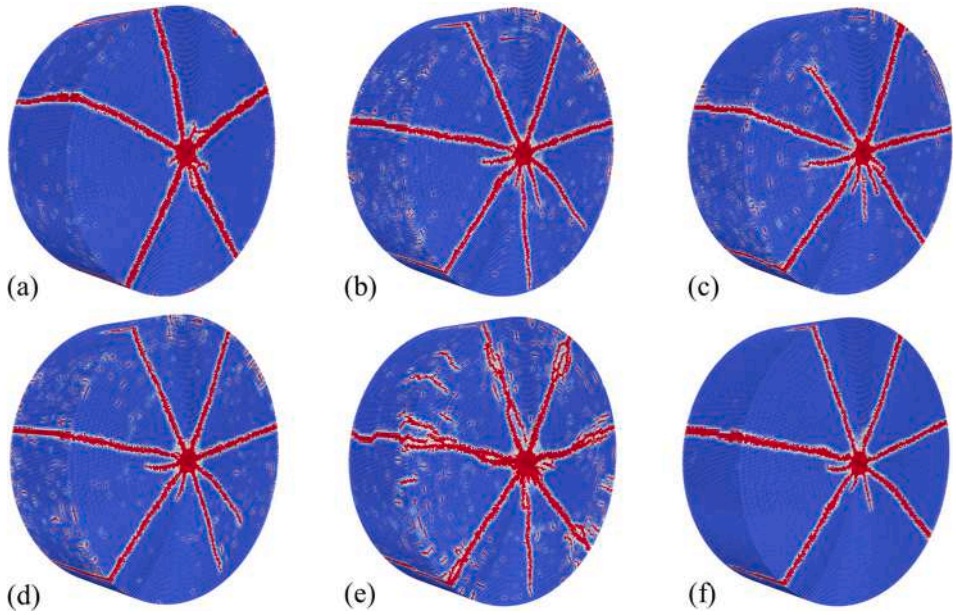


**Fig. 22.** Fracture pattern in the six sensitivity studies. Results for Case 1 through 6 are presented in (a) through (f). .

observed. The major radial cracks which extend to the outer boundary of the rock remain. The observation emphasises the importance of the tensile strength of material in modelling blasting induced fractures. In the present study a bilinear envelope (in the double log space) of tensile strength is assumed. The strain rate at which dynamic effect starts to accumulate, as well as the slope of the hardening curve, can be expected to play a vital role in the predicted fracture pattern. More detailed quantification of tensile material strength under varying strain rate is favoured for accurate simulation of blasting induced rock fractures. The above analyses is intended to offer an assessment on the influence of the key input parameters on the predicted fracture pattern. It should be noted that there are more than 25 input parameters in the present analysis and some of them (such as those in the JH2 model) are indeed correlated. One may resort to more rigorous quantitative approaches for sensitivity analysis, such as the probability sensitivity approach (Vu-Bac et al., 2016) which is capable to identify key input parameters for a specific output. This would require the output data to be well quantified with a sufficient output data set. It is beyond the scope of the current study but is considered an interesting topic to work on in the future.

## 4. Conclusions and outlook

This paper presents a peridynamics based computational approach for modelling blasting induced rock fractures. The approach features the application of a non-ordinary state-based peridynamics computational framework, with implementation of a JH2 constitutive model to consider the effect of large pressure, high strain rate, and viscoplasticity response of rock under blasting load. The failure of rock is gauged based on the JH2 model as well as a tension failure model – the former used to assess the plastic strain induced failure whereas the latter used to evaluate tensile failure. Detonation in the explosives is modelled using an updated Lagrangian formulation of peridynamics in conjunction with the JWL equation of state. The capacity of the proposed numerical approach is demonstrated with simulation of a single-hole blasting in granite rock. Parameter selection in the JH2 model and the tension failure model is discussed in comparison with those reported in the literature. The simulation results are shown to match with experimental observations in terms of fracture pattern, crack density and blasting induced pressures. The stability of simulation results is examined with different discretisation schemes. It is found that reducing the element size by 10% or increasing by 50% will all give reasonable fracture patterns and radial pressures in the simulated rock. However, with a coarser discretisation one may need to implement a stronger energy dissipation in the simulation to maintain numerical stability. Using adaptive discretisation in conjunction with the dual-horizon peridynamics formulation is also found to offer good results. A set of sensitivity studies have been carried out with adjusted parameters for the JH2 model and tension damage model. It is found that simulation results are not sensitive to the fracture strength parameters, the strain rate coefficient in the JH2 model as long as they are selected within the typical range of the material being investigated. The model is also not sensitive to the high order terms in the equation of state. Nonetheless, the intact strength parameters in the JH2 model are found to have notable influence the fracture pattern and should be selected with caution. Moreover, the tensile strength of material, as implemented in the tension damage model, appear to play a vital role in the fracture pattern. The tensile strength under varying strain rate should be determined with extra care when modelling blasting induced rock fractures.

Blasting involves various complex physical processes and there remain many phenomena that are not considered in the presented computational approach and could be incorporated in future studies. Notably, the explosive gas with extreme pressure and temperature may play a role in driving the growth of cracks (Kutter and Fairhurst, 1970), particularly in a stemmed explosion (Olsson et al.,

2002). An accurate simulation of the interaction between the explosive gas and the fractured rock is desirable. Coupled methods such as PD and SPH offers a potential solution for simulating such cases (Ren et al., 2014; Fan et al., 2016; Fan and Li, 2017). Using the combined total- and updated-Lagrangian formulation could also be a choice if the material instability can be well handled. In industrial operations, the detonation pressure could be much higher than that in a laboratory setting which results in more significant material distortion. The rock may also need to be simulated with the updated Lagrangian peridynamics formulation (Silling et al., 2017; Behzadinasab and Foster, 2020) for better handling of large deformation. It is straightforward to extend the presented computational approach to simulate industrial rock excavation where multiple interactive blasting operations are carried out and cracks experience intervening, branching, jointing, and arresting in a 3D domain. While the computational cost appears high, an adaptive refinement on the discretization in conjunction with a dual-horizon peridynamics formulation (Ren et al., 2016 & 2017) can potentially bring down the computational cost significantly. The advantage of peridynamics can be fully unleashed in handling those scenarios. More validation and benchmark simulations will be offered in future studies. For more accurate simulation and practical application, it would be desirable if the chemical, thermal, and mechanical processes of the detonation can be modelled explicitly so that different types of explosives, coupling media, and detonation features are taken into account with a more comprehensive, multi-physics-integrated computational framework.

## Credit author statement

**Fan Zhu**: Conceptualization, Methodology, Software, Validation, Formal analysis, Data curation, Visualization, Writing - original draft; **Jidong Zhao**: Supervision, Conceptualization, Analysis, Project administration, Writing - review & editing.

## Declaration of Competing Interest

The authors declare that they have no known competing financial interests or personal relationships that could have appeared to influece the work reported in this paper.

## Acknowledgments

The study was financially supported by the National Science Foundation of China under project 11972030 and Research Grants Council of Hong Kong through GRF project 16208720.

## References

Banadaki, M.M.D., 2010. Stress-wave Induced Fracture in Rock Due to Explosive action. Doctoral dissertation. University of Toronto.
Banadaki, M.M.D., Mohanty, B., 2012. Numerical simulation of stress wave induced fractures in rock. Int. J. Impact. Eng. 40–41, 16–25.
Baranowski, P., Kucewicz, M., Gieleta, R., Stankiewicz, M., Konarzewski, M., Bogusz, P., Pytlik, M., Małachowski, J., 2020. Fracture and fragmentation of dolomite rock using the JH-2 constitutive model: parameter determination, experiments and simulations. Int. J. Impact Eng., 103543
Bauer, A., Calder, P.N., 1978. Open Pit and Blasting Seminar. Mining Engineering Dept. Queens University, Kinston Ontario.
Baydoun, M., Fries, T.P., 2012. Crack propagation criteria in three dimensions using the XFEM and an explicit-implicit crack description. Int. J. Fract. 178 (1), 51–70.
Behzadinasab, M., Foster, J.T., 2020. A semi-Lagrangian constitutive correspondence framework for peridynamics. J. Mech. Phys. Solids 137, 103862.
Bergel, G.L., Li, S., 2016. The total and updated lagrangian formulations of state-based peridynamics. Comput. Mech. 58, 351–370.
Børvik, T., Olovsson, L., Hanssen, A.G., Dharmasena, K.P., Hansson, H., Wadley, H.N.G., 2011. A discrete particle approach to simulate the combined effect of blast and sand impact loading of steel plates. J. Mech. Phys. Solids 59 (5), 940–958.
Butt, S.N., Timothy, J.J., Meschke, G., 2017. Wave dispersion and propagation in state-based peridynamics. Comput. Mech. 60, 725–738.
Cho, S.H., Kaneko, K., 2004. Influence of the applied pressure waveform on the dynamic fracture processes in rock. Int. J. Rock Mech. Min. Sci. 41, 771–784.
Cho, S.H., Ogata, Y., Kaneko, K., 2003. Strain-rate dependency of the dynamic tensile strength of rock. Int. J. Rock Mech. Min. Sci. 40, 763–777.
Daehnke, A., Rossmanith, H.P., Schatz, J.F., 1997. On dynamic gas pressure induced fracturing. Fragblast 1, 73–97.
Deng, X.F., Zhu, J.B., Chen, S.G., Zhao, Z.Y., Zhou, Y.X., Zhao, J., 2014. Numerical study on tunnel damage subject to blast-induced shock wave in jointed rock masses. Tunn. Undergr. Sp. Tech. 43, 88–100.
Donzé, F.V., Bouchez, J., Magnier, S.A., 1997. Modeling fractures in rock blasting. Int. J. Rock Mech. Min. Sci. 34 (8), 1153–1163.
Drukovanyi, M.F., Kravtsov, V.S., Chernyavskii, Y.E., Shelenok, V.V., Reva, N.P., Zver'kov, S.N., 1976. Calculation of fracture zones created by exploding cylindrical charges in ledge rocks. Soviet Min. Sci. 12, 292–295.
Fan, H., Bergel, G.L., Li, S., 2016. A hybrid Peridynamics-SPH simulation of soil fragmentation by blast loads of buried explosive. Int. J. Impact. Eng. 87, 14–27.
Fan, H., Li, S., 2017. A Peridynamics-SPH modeling and simulation of blast fragmentation of soil under buried explosive loads. Comput. Methods. Appl. Mech. Engrg. 318, 349–381.
Flanagan, D.P., Taylor, L.M., 1987. An accurate numerical algorithm for stress integration with finite rotations. Comput. Methods. Appl. Mech. Engrg. 62, 305–320.
Foster, J.T., Silling, S.A., Chen, W., 2011. An energy based failure criterion for use with peridynnamic states. Int. J. Multiscale Comput. Eng. 9 (6), 675–688.
Gao, C., Zhou, Z., Li, Z., Li, L., Cheng, S., 2020. Peridynamics simulation of surrounding rock damage characteristics during tunnel excavation. Tunn. Undergr. Space. Technol. 97, 103289.
Gharehdash, S., Barzegar, M., Palymskiy, I.B., Fomin, P.A., 2020. Blast induced fracture modelling using smoothed particle hydrodynamics. Int. J. Impact. Eng. 135, 103235.
Holmberg, R., Persson, P.A., 1978. The Swedish approach to contour blasting. Proc. IVth Conf. on Exp. and Blasting Tech. ISEE, New Orleans, LA, 113–127.
Holmberg, R., Persson, P.A., 1980. Design of tunnel perimeter blasting patterns to prevent rock damage. Trans. Inst. Min. Metall, London 89, A37–A40.
Holmquist, T.J., Johnson, G.R., Cook, W.H., 1993. A computational constitutive model for concrete subjected to large strains, high strain rates, and high pressures. In: Proceedings of the 14th international symposium on ballistics, pp. 591–600.
Hustrulid, W., 2010. Some comments regarding development drifting practices with special emphasis on caving applications. In: Potvin, Y (Ed.), Proceedings of the Second International Symposium on Block and Sublevel Caving. Australian Centre for Geomechanics, Perth, pp. 3–43.
Johnson, G.R., Holmquist, T.J., 1994. An improved computational constitutive model for brittle materials. AIP Conf. Proc. 309 (1), 981–984.
Kutter, H.K., Fairhurst, C., 1970. On the fracture process in blasting. Int. J. Rock Mech. Min. Sci. 8, 181–202.
Lai, X., Liu, L., Li, S., Zeleke, M., Liu, Q., Wang, Z., 2018. A non-ordinary state-based peridynamics modeling of fractures in quasi-brittle materials. Int. J. Impact. Eng. 111, 130–146.

Lai, X., Ren, B., Fan, H., Li, S., Wu, C.T., Regueiro, R.A., Liu, L., 2015. Peridynamics simulations of geomaterial fragmentation by impulse loads. Int. J. Numer. Anal. Methods. Geomech. 39 (12), 1304–1330.
Lanari, M., Fakhimi, A., 2015. Numerical study of contributions of shock wave and gas penetration toward induced rock damage during blasting. Comp. Part. Mech. 2, 197–208.
Lee, C.W., Kim, J., Kang, G.C., 2018. Full-scale tests for assessing blasting-induced vibration and noise. Shock Vib. 2018, 9354349.
Littlewood, D.J., 2011. A nonlocal approach to modeling crack nucleation in AA 7075-T651. ASME 2011 international mechanical engineering congress and exposition. Am. Soc. Mech. Eng. 567–576.
Liu, M.B., Liu, G.R., 2016. Particle Methods for Multi-Scale and Multi-Physics. World Scientific Publishing Co. Inc.
Ma, G.W., An, X.M., 2008. Numerical simulation of blasting-induced rock fractures. Int. J. Rock. Mech. Min. Sci. 45, 966–975.
Madenci, E., Oterkus, E., 2014. Peridynamic Theory and Its Applications. Springer, New York.
Mojitabai, N., Beatie, S.G., 1996. Empirical approach to prediction of damage in bench blasting. Trans. Inst. Min. Metall. Sect. 105, 75–80.
Monaghan, J.J., 1987. SPH Meets the Shocks of NOH. Department of Mathematics, Monash University.
Olsson, M., Nie, S., Bergqvist, I., Ouchterlony, F., 2002. What causes cracks in rock blasting? Fragblast 6 (2), 221–233.
Rabczuk, T., Belytschko, T., 2007. A three-dimensional large deformation meshfree method for arbitrary evolving cracks. Comput. Methods Appl. Mech. Engrg. 196, 2777–2799.
Rabczuk, T., Ren, H., 2017. A peridynamics formulation for quasi-static fracture and contact in rock. Engng. Geol. 225 (20), 42–48.
Rabczuk, T., Zi, G., Bordas, S., Xuan, H.N., 2010. A simple and robust three-dimensional cracking-particle method without enrichment. Comput. Methods Appl. Mech. Engrg. 199, 2437–2455.
Ren, B., Fan, H., Bergel, G.L., Regueiro, R.A., Lai, X., Li, S., 2014. A peridynamics-SPH coupling approach to simulate soil fragmentation induced by shock waves. Comput. Mech. 55, 287–302.
Ren, H., Zhuang, X., Cai, Y., Rabczuk, T., 2016. Dual-horizon peridynamics. Int. J. Numer. Methods. Engrg. 108, 1451–1476.
Ren, H., Zhuang, X., Rabczuk, T., 2017. Dual-horizon peridynamics: a stable solution to varying horizons. Comput. Methods Appl. Mech. Engrg. 318, 762–782.
Ren, H., Zhuang, X., Rabczuk, T., 2020. A nonlocal operator method for solving partial differential equations. Comput. Methods Appl. Mech. Engrg. 358, 112621.
Shou, Y., Zhou, X., Berto, F., 2019. 3D numerical simulation of initiation, propagation and coalescence of cracks using the extended non-ordinary state-based peridynamics. Theor. Appl. Fract. Mech. 101, 254–268.
Silling, S.A., 2000. Reformulation of elasticity theory for discontinuities and long-range forces. J. Mech. Phys. Solids 48 (1), 175–209.
Silling, S.A., Askari, E., 2005. A meshfree method based on the peridynamic model of solid mechanics. Comput. Struct. 83 (17–18), 1526–1535.
Silling, S.A., Epton, M., Weckner, O., Xu, J., Askari, A., 2007. Peridynamics states and constitutive modeling. J. Elasticity 88 (2), 151–184.
Silling, S.A., Parks, M.L., Kamm, J.R., Weckner, O., Rassaian, M., 2017. Modeling shockwaves and impact phenomena with Eulerian peridynamics. Int. J. Impact. Eng. 107, 47–57.
Sundaram, B.M., Tippur, H.V., 2018. Dynamic fracture of soda-lime glass: a full-field optical investigation of crack initiation, propagation and branching. J. Mech. Phys. Solids 120, 132–153.
Taylor, L.M., Chen, E.P., Kuszmaul, J.S., 1986. Microcrack-induced damage accumulation in brittle rock under dynamic loading. Comput. Meth. Appl. Mech. Eng. 55 (3), 301–320.
Tesarik, D.R., Hustrulid, W.A., Nyberg, U., 2011. Assessment and application of a single-charge blast test at the Kiruna mine. Sweden. Blast. Fragment. 5 (1), 47–72.
Tupek, M.R., Radovitzky, R., 2014. An extended constitutive correspondence formulation of peridynamics based on nonlinear bond-strain measures. J. Mech. Phys. Solids 65, 82–92.
Vu-Bac, N., Lahmer, T., Zhuang, X., Nguyen-Thoi, T., Rabczuk, T., 2016. A software framework for probabilistic sensitivity analysis for computationally expensive models. Adv. Eng. Softw. 100, 19–31.
Wang, J., Yin, Y., Esmaieli, K., 2018. Numerical simulations of rock blasting damage based on laboratory-scale experiments. J. Geophys. Eng. 15, 2399–2417.
Warren, T.L., Silling, S.A., Askari, A., Weckner, O., Epton, M.A., Xu, J., 2009. A non-ordinary state-based peridynamic method to model solid material deformation and fracture. Int. J. Solids Struct. 46, 1186–1195.
Wei, X.Y., Zhao, Z.Y., Gu, J., 2009. Numerical simulations of rock mass damage induced by underground explosion. Int. J. Rock. Mech. Min. Sci. 46, 1206–1213.
Xiao, S.P., Belytschko, T., 2005. Material stability analysis of particle methods. Adv. Comput. Math. 23, 171–190.
Xie, L.X., Yang, S.Q., Gu, J.C., Zhang, Q.B., Lu, W.B., Jing, H.W., Wang, Z.L., 2019. JHR constitutive model for rock under dynamic loads. Comput. Geotechnic. 108, 161–172.
Yi, C., Sjöberg, J., Johansson, D., 2017. Numerical modelling for blast-induced fragmentation in sublevel caving mines. Tunn. Undergr. Sp. Tech. 68, 167–173.
Zárate, F., Gonzalez, J.M., Miquel, J., Löhner, R., Oñate, E., 2018. A coupled fluid FEM-DEM technique for predicting blasting operations in tunnels. Underground Space 3 (4), 310–316.
Zhang, Z.X., 2016. Rock Fracture and Blasting: Theory and Applications. Elsevier Inc.
Zhu, F., Zhao, J., 2019. A peridynamic investigation on crushing of sand particles. Géotechnique 69 (6), 526–540.
Zhu, F., Zhao, J., 2020. Multiscale modeling of continuous crushing of granular media: the role of grain microstructure. Comput. Part. Mech. https://doi.org/10.1007/s40571-020-00355-0. In press.